*Article*

# The Solar Energy Potential of Greece for Flat-Plate Solar Panels Fixed on Dual-Axis Systems

**Harry D. Kambezidis [1,2,*,&,&&], Konstantinos Mimidis [3,%], Kosmas A. Kavadias [2,#]**

[1] Atmospheric Research Team, Institute of Environmental Research and Sustainable Development, National Observatory of Athens, Lofos Nymphon, GR-11810 Athens, Greece
[2] Soft Energy Systems and Environmental Protection Laboratory, Department of Mechanical Engineering, University of West Attica, P. Ralli & Thivon 250, GR-12244 Egaleo, Greece
[3] Municipality of Ancient Olympia, Ch. Kosmopoulou 1, GR-27065 Ancient Olympia, Greece
[&] Emeritus Researcher; harry@noa.gr
[&&] Research Associate; harry@uniwa.gr
[%] Civil and Environmental Engineer; kosmim@hotmail.com
[#] Associate Professor; kosmas.kavadias@uniwa.gr
[*] Correspondence: harry@noa.gr

**Abstract:** The objective of the present work is to investigate the performance of flat-plate solar panels in Greece that continuously follow the daily motion of the Sun. To that end, the annual energy sums are estimated on such surfaces from hourly solar horizontal radiation values at 43 locations covering all of Greece. The solar horizontal radiation values are embedded in the typical meteorological years of the sites obtained from the PV-GIS tool. All calculations use a near-real surface albedo; an isotropic and an anisotropic model are used to estimate the diffuse-inclined radiation. The analysis provides regression equations for the energy sums as a function of time (month, season). The annual energy sums are found to vary between 2247 kWhm$^{-2}$ and 2878 kWhm$^{-2}$ under all-sky conditions with the anisotropic transposition model. Finally, maps of Greece showing the distribution of the annual and seasonal solar energy sums under all- and clear-sky conditions are derived for the first time.

**Keywords:** solar energy potential; maximum energy; inclined surfaces; solar tracking; Greece

## 1. Introduction

Installations with tilted solar panels exploiting solar energy have long existed in the market. Solar flat-plate panels are widely used to convert solar energy into electricity (e.g., PV installations). These systems consist of solar collectors receiving solar radiation on flat-plate surface(s) that can operate in three different modes: (i) at a fixed-tilt angle with southward orientation in the northern hemisphere or northward orientation in the southern hemisphere, (ii) at a fixed-tilt angle rotated on a vertical axis (one-axis or single-axis) system that continuously follows the Sun, and (iii) at a varying-tilt angle fixed on a two-axis (or dual-axis) system that continuously tracks the Sun. Installations of mode-(i) are known as fixed-tilt systems and are widely used because of their lower installation and maintenance costs. Installation of mode-(ii) systems provide higher solar energy on the inclined surface but have a slightly higher cost because of the necessary maintenance of the moving parts. Installation of mode-(iii) systems is considered the most effective because the solar rays are always normal to the receiving flat-plate surface. These systems provide higher performance, but they are, though, associated with higher maintenance costs because of more moving parts. The first type of solar system is also called stationary or static, while the other two are named dynamic, because of their Sun-tracking ability. Recently, Kambezidis and Psiloglou [1] examined the mode-(i) static systems for the performance of fixed-tilt flat-plate solar collectors with southward orientation in Greece, but investigation of the solar energy potential across the country for mode-(ii) and -(iii) systems has never been

Preprints (www.preprints.org) | NOT PEER-REVIEWED | Posted: 8 May 2023 doi:10.20944/preprints202305.0488.v1

made. The present work investigates the mode-(iii) dynamic systems for the solar energy potential received on flat-plate solar collectors for the first time in Greece.

Static solar systems are nowadays widely used in solar energy applications worldwide because of their simple construction and low maintenance cost. For this reason, they have received great attention from researchers (c.f., solar energy potential, solar availability) at a certain location or region, e.g., [2-5]. Another priority has been given to dynamic mode-(ii) solar systems because of their relatively higher solar energy imprint, e.g., [6]. As far as the dynamic mode-(iii) solar systems are concerned, they have started being used in the last 20 years because of their higher performance compared to that of the other two types, e.g., [7,8]. Much effort has been invested, though, in improving both moving and electronic parts for the Sun-tracking sensors, e.g., [3,9], which are involved in the configuration of dynamic solar systems. Nevertheless, the performance of such systems must be evaluated against solar radiation measurements at first-hand, e.g., [10]. However, the scarcity of solar radiation measuring stations worldwide has triggered the development of solar radiation modelling, e.g., [11,12,13], to derive the optimum tilt angle and orientation for obtaining maximum solar energy on flat-plate solar panels for static systems in both hemispheres. Other methods use a combination of ground-based solar data and modelling, e.g., [14], or utilise solar data from international databases, e.g., [15,16].

Some studies, like the present work, have already been conducted in Greece. Tsalides and Thanailakis [17] computed the optimum azimuth and tilt angles of PV arrays at 9 locations in Greece; they found that PV arrays having azimuth angles in the range ±30° (0° at south) receive about 40% - 60% greater solar energy than that for tilt angles equal to the latitude of the sites. Koronakis [18] found an optimum tilt angle of 25° toward the south for flat-plate collectors and 30° for concentrated solar cells at Athens all-year round. Balouktsis et al. [19] analysed the optimal tilt angle of PV installations at certain locations in Greece and found it to be around 25° to the south. Synodinou and Katsoulis [20] estimated a tilt angle equal to the latitude of Athens for optimum solar energy harvesting at this location. Darhmaoui and Lahjouji [21], by analysing the solar radiation databases of 35 sites around the Mediterranean, found the optimum tilt angles with south orientation; for Irakleio, Athens, and Mikra in Greece; these angles were estimated at 35.1°, 36.8°, and 38.7°, respectively. Kaldellis et al. [22] found an optimum tilt angle for south-oriented surfaces in Athens and central Greece of 15° during the summer. Jacobson and Jadhav [23] have derived a review for the optimum tilt angles with south orientation in the northern hemisphere by using the PV-Watts algorithm; for Athens, they estimated it at 29°. Raptis et al. [24] estimated the optimum tilt angle for maximum energy reception on flat-plate collectors with south orientation in Athens at 39°. Recently, Kambezidis and Psiloglou [1] suggested a new methodology for estimating the optimum tilt angle for south-oriented flat-plate solar collectors in Greece; by applying the method, they found the optimum tilt angles in the range of 25° - 30°, thus agreeing with the results of Koronakis, Balouktsis et al., and Jacobson and Jadhav. In 1996, the European Solar Radiation Atlas was derived [25] and published in 2001 [26]; it includes maps of the solar energy potential on horizontal and inclined surfaces over almost all of Europe, including Greece; the maps were derived from solar radiation databases across the continent covering the period 1981 - 1990 with a resolution of 10 km. Also, a Global Solar Atlas has been generated [27] for almost all of the world, including Greece. These maps concern global solar horizontal irradiation, direct-normal solar irradiation, and PV power potential. Calculations for these maps were made by using data in the periods 1994, 1999, 2007 - 2018 depending on the region. Moreover, a map of the solar potential over Greece on horizontal plane based on typical meteorological years (TMYs) was developed by Kambezidis et al. [28]. Finally, a study about the future solar resource in Greece due to climate change has appeared in the literature [29].

From the above, it is clear that an attempt has yet to be made to construct a solar map for Greece to show the solar energy potential on inclined flat-plate surfaces that continuously track the Sun. This gap is bridged in the present study; for the first time, solar maps for Greece showing the energy on inclined flat-plate surfaces tracking the Sun are derived.

The structure of the paper is the following. Section 2 describes the data collection and data analysis. Section 3 deploys the results of the study. Section 4 provides a discussion, and Section 5 presents the conclusions and main achievements of the work. Acknowledgements and References follow.

Preprints (www.preprints.org) | NOT PEER-REVIEWED | Posted: 8 May 2023 doi:10.20944/preprints202305.0488.v1

## 2. Materials and Methods

### *2.1. Data Collection*

Hourly values of solar radiation were downloaded from the PV—Geographical Information System (PV-GIS) tool [30] using the Surface Solar Radiation Data Set-Heliostat (SARAH) 2005 - 2016 database (12 years) [31,32]. The PV-GIS platform provides solar radiation data through a user-friendly tool for almost any location in the world, including Greece. The methodology used for estimating solar radiation from satellites by the PV-GIS tool is described in various works, e.g., [33,34].

In the present work, a set of 43 sites was arbitrarily chosen to cover the whole territory of Greece. The location of these sites has been adopted from a recent work on the solar radiation climate of Greece [14]. Table 1 provides the names and geographical coordinates of the sites; Figure 1 shows their location on the map of Greece.

TMYs for the above sites were downloaded from the PV-GIS tool; these TMYs include hourly values of air temperature (in degrees C), relative humidity (in %), horizontal infra-red radiation (in $Wm^{-2}$), wind speed (in $ms^{-1}$) and direction (in degrees), surface pressure (in Pa), global horizontal irradiance, $H_g$ (in $Wm^{-2}$), direct-normal solar irradiance, $H_{bn}$ (in $Wm^{-2}$), and diffuse horizontal irradiance, $H_d$ (in $Wm^{-2}$). The latter three parameters were considered in this study. The TMYs were derived in the PV-GIS platform from simulations from 2005 to 2016.

**Table 1.** The 43 sites selected over Greece to cover the whole area of the country. This Table is a reproduction of Table 1 in [14]. φ = geographical latitude, and λ = geographical longitude (both in the WGS84 geodetic system); z = altitude; N = North of equator; E = East of Greenwich meridian; amsl = above mean sea level.

| Site number | Site name / Region / z (m amsl) | λ (° E) | φ (° N) |
|---|---|---|---|
| 1 | Agrinio/Western Greece/25 | 21.383 | 38.617 |
| 2 | Alexandroupoli/Eastern Macedonia and Thrace/3.5 | 25.933 | 40.850 |
| 3 | Anchialos/Thessaly/15.3 | 22.800 | 39.067 |
| 4 | Andravida/Western Greece/15.1 | 21.283 | 37.917 |
| 5 | Araxos/Western Greece/11.7 | 21.417 | 38.133 |
| 6 | Arta/Epirus/96 | 20.988 | 39.158 |
| 7 | Chios/Northern Aegean/4 | 26.150 | 38.350 |
| 8 | Didymoteicho/Eastern Macedonia and Thrace/27 | 26.496 | 41.348 |
| 9 | Edessa/Western Macedonia/321 | 22.044 | 40.802 |
| 10 | Elliniko/Attica/15 | 23.750 | 37.900 |
| 11 | Ioannina/Epirus/484 | 20.817 | 39.700 |
| 12 | Irakleio/Crete/39.3 (also written as Heraklion) | 25.183 | 35.333 |
| 13 | Kalamata/Peloponnese/11.1 | 22.000 | 37.067 |
| 14 | Kastelli/Crete/335 | 25.333 | 35.120 |
| 15 | Kastellorizo/Southern Aegean/134 | 29.576 | 36.142 |
| 16 | Kastoria/Western Macedonia/660.9 | 21.283 | 40.450 |
| 17 | Kerkyra/Ionian Islands/4 (also known as Corfu) | 19.917 | 39.617 |
| 18 | Komotini/Eastern Macedonia and Thrace/44 | 25.407 | 41.122 |
| 19 | Kozani/Western Macedonia/625 | 21.783 | 40.283 |
| 20 | Kythira/Attica/166.8 | 23.017 | 36.133 |
| 21 | Lamia/Sterea Ellada/17.4 | 22.400 | 38.850 |
| 22 | Larissa/Thessaly/73.6 | 22.450 | 39.650 |
| 23 | Lesvos/Northern Aegean/4.8 | 26.600 | 39.067 |
| 24 | Limnos/Northern Aegean/4.6 | 25.233 | 39.917 |
| 25 | Methoni/Peloponnese/52.4 | 21.700 | 36.833 |
| 26 | Mikra/Central Macedonia/4.8 | 22.967 | 40.517 |

Preprints (www.preprints.org) | NOT PEER-REVIEWED | Posted: 8 May 2023 doi:10.20944/preprints202305.0488.v1

| | | |
|---|---|---|
| 27 | Milos/Southern Aegean/5 | 24.475 36.697 |
| 28 | Naxos/Southern Aegean/9.8 | 25.533 37.100 |
| 29 | Orestiada/Eastern Macedonia and Thrace/41 | 26.531 41.501 |
| 30 | Rodos/Southern Aegean/11.5 (also written as Rhodes) | 28.117 36.400 |
| 31 | Samos/Northern Aegean/7.3 | 26.917 37.700 |
| 32 | Serres/Central Macedonia/34.5 | 23.567 41.083 |
| 33 | Siteia/Crete/115.6 | 26.100 35.120 |
| 34 | Skyros/Sterea Ellada/17.9 | 24.550 38.900 |
| 35 | Souda/Crete/140 | 21.117 35.550 |
| 36 | Spata/Attica/67 | 23.917 37.967 |
| 37 | Tanagra/Sterea Ellada/139 | 23.550 38.317 |
| 38 | Thira/Southern Aegean/36.5 | 25.433 36.417 |
| 39 | Thiva/Sterea Ellada/189 | 23.320 38.322 |
| 40 | Trikala/Thessaly/114 | 21.768 39.556 |
| 41 | Tripoli/Peloponnese/652 | 22.400 37.533 |
| 42 | Xanthi/Eastern Macedonia and Thrace/83 | 24.886 41.130 |
| 43 | Zakynthos/Ionian Islands/7.9 (also known as Zante) | 20.900 37.783 |

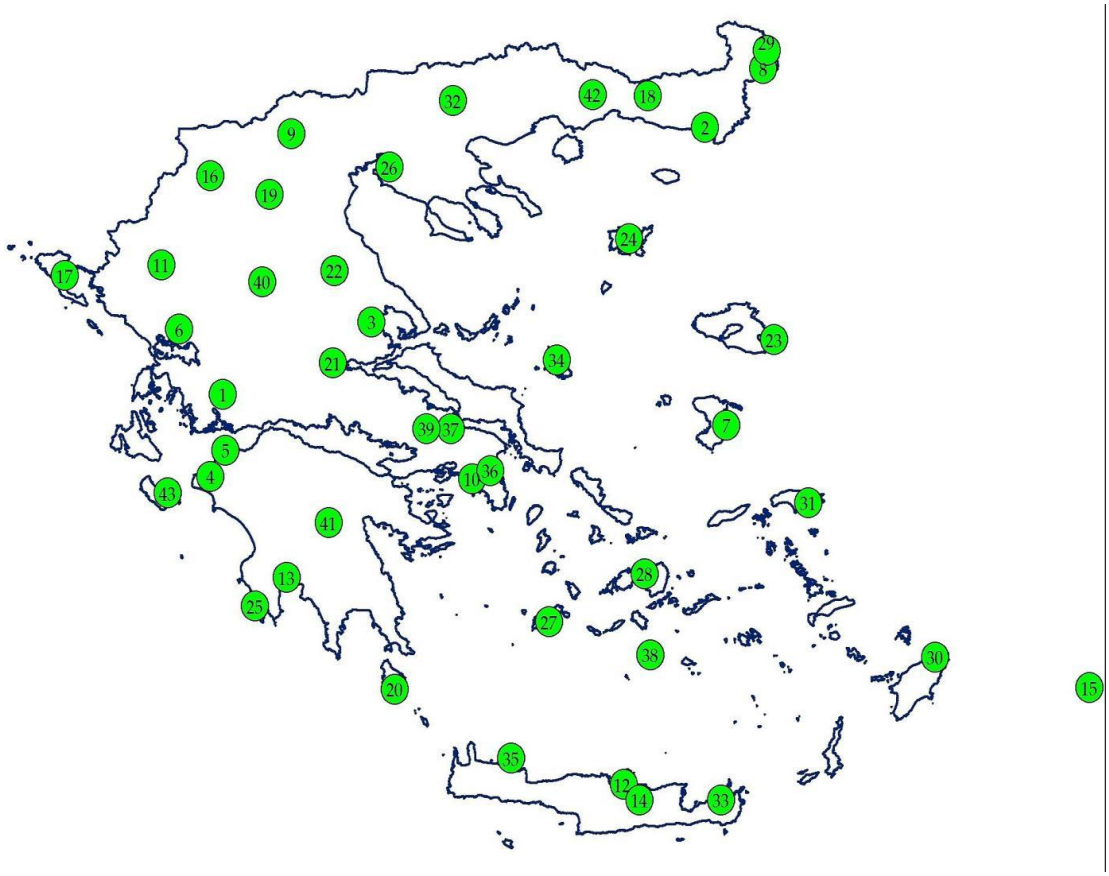


**Figure 1.** Distribution of the 43 selected sites in Greece. The numbers in the circles refer to those in column 1 of Table 1. This Figure is a reproduction of Figure 1 in [14].

*2.2. Data Processing and Analysis*

To process the data used in this work, the following 5 steps were followed.

Step 1. The downloaded hourly data from the PV-GIS website were transferred from universal time coordinate (UTC) into Greek local standard time (LST = UTC + 2 h). It must be mentioned that

Preprints (www.preprints.org) | NOT PEER-REVIEWED | Posted: 8 May 2023 doi:10.20944/preprints202305.0488.v1

the PV-GIS solar radiation values were provided at different UTC times for the 43 sites considered, e.g., at hh:48 or hh:09, where hh stands for any hour between 00 and 23.

Step 2. The routine SUNAE introduced by Walraven [35] was used to derive the solar azimuths and elevations. However, the original SUNAE algorithm has been renamed to XRONOS (meaning time in Greek, X is pronounced CH) because of added modifications due to the right ascension and atmospheric refraction effects [36,37]. XRONOS ran for the geographical coordinates of the 43 sites in their TMYs to derive the solar altitudes, $\gamma$, at all LST times calculated in step 1. Nevertheless, inconsistencies (gaps) in the solar azimuth angles, $\psi$, at both instances of sunrise and sunset were found during calculations in the XRONOS code. The discrepancy was overcome by implementing a modified XRONOS (mXRONOS) code in MatLab; a Fourier series approximation of the expression for $\psi$ at the sunrise and sunset instances was derived and applied to all 43 sites. The mXRONOS algorithm is described in detail in an article recently published in the journal of Sun and Geosphere [38].

Step 3. The hourly direct horizontal solar radiation, $H_b$, values were estimated at all sites by the expression $H_b = H_{bn} \cdot \sin\gamma$.

Step 4. All solar radiation and solar geometry values were assigned to the nearest LST hour (i.e., values at hh:48 LST or hh:09 LST were assigned to hh:00 LST). That was done to have all values in the database as integer hours.

Step 5. Only those hourly solar radiation values greater than 0 $Wm^{-2}$ and corresponding to $\gamma \geq 5°$ (to avoid the cosine effect) were retained for further analysis. Also, the criterion of $H_d \leq H_g$ was required to be met at hourly level.

For estimating global solar irradiance on a flat-plate solar collector fixed on a dual-axis system that continuously tracks the Sun, $H_{g,t}$ (in $Wm^{-2}$), the isotropic model of Liu-Jordan (L-J) [39], as well as the anisotropic model of Hay [40,41], was adopted (the subscript t stands for "tracking"). The isotropic and anisotropic models were used to estimate (i) the ground-reflected radiation from the surrounding surface, $H_{r,t}$ (in $Wm^{-2}$), and (ii) the diffuse inclined radiation, $H_{d,t}$ (in $Wm^{-2}$), received on the sloping flat-plate surface. These models were adopted in the present study because of their simplicity and effectiveness in providing the tilted total solar radiation; a second reason for using both transposition models was to compare their results. The satisfactory performance of the L-J and Hay models has been verified by various studies, e.g., [42,43].

Figure 2 provides a schematic for a tilted surface receiving solar radiation. Deliberately, the tilted surface is not aligned along the direction of the Sun to show the various angles formed, i.e., the tilt angle of the surface, $\beta$, the solar altitude, $\gamma$, the incidence angle, $\theta$ (the angle between the normal to the surface and the direction toward the Sun), the solar azimuth, $\psi$, and the azimuth of the tilted plane, $\psi'$.

Preprints (www.preprints.org) | NOT PEER-REVIEWED | Posted: 8 May 2023 doi:10.20944/preprints202305.0488.v1

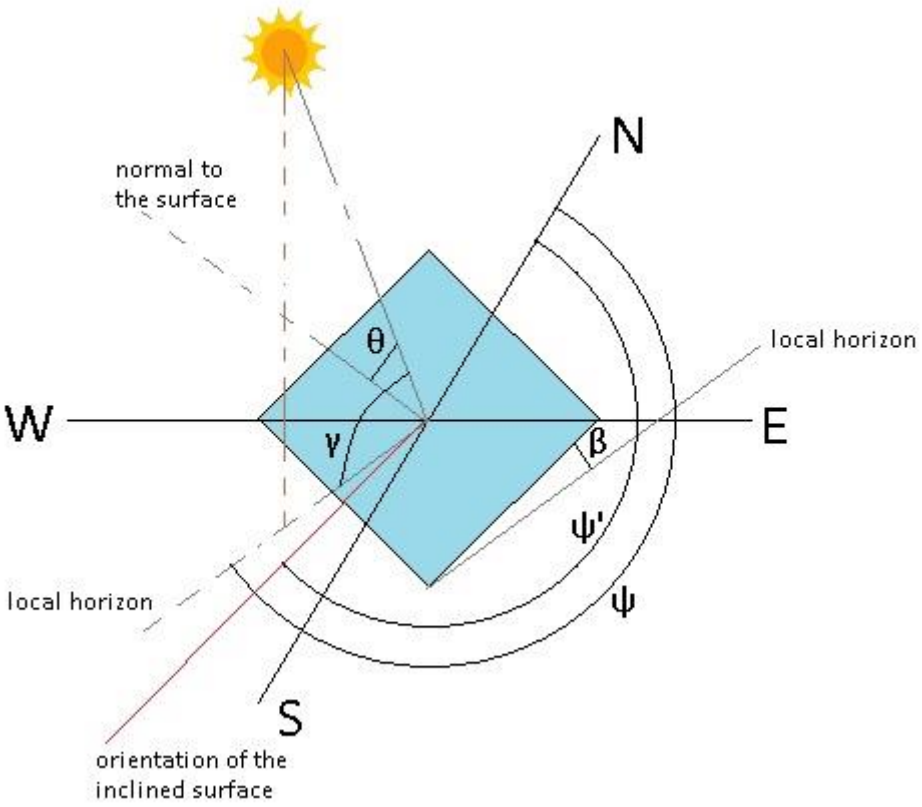


**Figure 2.** Inclined surface (of a PV array) at a tilt angle β with arbitrary orientation. E, W, N, S denote East, West, North, and South, respectively. Also, the solar altitude, γ, the solar azimuth, ψ, the tilted surface's azimuth, ψ', and the incidence angle, θ, are shown.

For a Sun-tracking surface the received total solar radiation is given by the following well-known expression:

$$H_{g,t} = H_{b,t} + H_{d,t} + H_{r,t}\ [44], \quad (1)$$

The solar radiation components in Equation (1) are calculated by the following analytical expressions:

$$H_{r,t} = H_g \cdot R_r \cdot \varrho_g\ [44], \quad (2)$$

$$R_r = (1 - \cos\beta)/2 = (1 - \sin\gamma)/2\ [44], \quad (3)$$

$$H_{d,t} = H_d \cdot R_{d,model}, \text{ (model = L-J or Hay) } [44], \quad (4a)$$

$$R_{d,L\text{-}J} = (1 + \cos\beta)/2 = (1 + \sin\gamma)/2\ [39], \quad (4b)$$

$$R_{d,Hay} = K_b \cdot R_b + (1 - K_b) \cdot R_{d,L\text{-}J}\ [40,41], \quad (4c)$$

$$R_b = \max(\cos\theta/\sin\gamma, 0)\ [40,41], \quad (4d)$$

$$K_b = \min(H_b/H_{ex}, 1)\ [40,41], \quad (4e)$$

$$H_{b,t} = H_b \cdot \cos\theta/\sin\gamma = H_b \cdot \cos 0/\sin\beta = H_b/\cos\gamma\ [44], \quad (5)$$

$$\cos\theta = \sin\beta \cdot \cos\gamma \cdot \cos(\psi - \psi') + \cos\beta \cdot \sin\gamma\ [45], \quad (6)$$

$$H_{ex} = H_0 \cdot S \cdot \sin\gamma\ [45], \quad (7)$$

$$H_0 = 1361.1\ \text{Wm}^{-2} \text{ (recent solar constant [46])}, \quad (8)$$

$$S = 1 + 0.033 \cdot \cos(2 \cdot \pi \cdot N/365)\ [47], \quad (9)$$

$$H_{b,t} = H_b \cdot \cos\theta/\sin\gamma = H_b \cdot \cos 0/\sin\beta = H_b/\cos\gamma\ [44], \quad (10)$$

where, in this case, $\theta = 0^o$ and $\beta = 90^o - \gamma$ because the inclined surface is always normal to the solar rays (see Figure 2); also, $\psi = \psi'$, because of the Sun-tracking feature of the mode-(iii) system. $R_d$ and $R_r$ are the sky-configuration and ground-inclined plane-configuration factors, respectively, S is the Sun-Earth distance correction factor, and N is the day number of the year (N = 1 for 1 January, and N = 365 for 31 December in a non-leap year or N = 366 in a leap year). In the L-J model the ground albedo

Preprints (www.preprints.org) | NOT PEER-REVIEWED | Posted: 8 May 2023 doi:10.20944/preprints202305.0488.v1

usually takes the value of $\varrho_{g0} = 0.2$ (Equation (2)). Nevertheless, in the present study this value has been replaced with the near-real ground-albedo one, $\varrho_g$, for all 43 sites. To retrieve the $\varrho_g$ values for the 43 sites, use of the Giovanni portal [48] was made; pixels of 0.5° × 0.625° spatial resolution were centered over each of the 43 sites for which monthly mean values of the ground albedo were downloaded in the period 2005 - 2016. Monthly mean $\varrho_g$ values were then computed for all sites and were used to calculate $H_{g,t}$.

To isolate those solar radiation values that corresponded to clear-sky conditions only, use of the modified clearness index, $k'_t$, was made as in [49]. The significance of this modified index is that it does not depend on air mass [50]. Its definition is the following:

$$k'_t = \frac{k_t}{0.1 + 1.031 \cdot exp\left[-1.4 \Big/ \left(0.9 + \frac{9.4}{m}\right)\right]}, \quad (11)$$

$$m = 1 \Big/ \left[\sin\gamma + 0.50572\,(\gamma + 6.07995)^{-1.6364}\right]\ [51], \quad (12)$$

$$k_t = H_g \Big/ S \cdot H_0 \cdot \sin\gamma, \quad (13)$$

where m is the optical air mass. Kambezidis and Psiloglou [49] have defined the range for clear skies as $0.65 < k'_t \leq 1$. This range has been used in the present study, while the all-sky conditions are characterised by the full range of $0 < k'_t \leq 1$. The atmospheric extinction index, $k_e$, from [52] was adopted; it is defined as $k_e = H_d/H_b$ [53]. Its meaning is that it gives information about the percentage contribution of both the $H_d$ and $H_b$ solar radiation components to solar applications over an area and, more specifically, to PV installations. In other words, it denotes the significant fractional amount of each solar component in solar harvesting.

For every site, hourly values of $H_{g,t}$ were estimated twice from Equation (1); the first time by using Equations (4a, 4b) for the L-J model and the second time by using Equations (4a – 4e) for the Hay model. From the hourly $H_{g,t}$ values, annual, seasonal, and monthly solar energy sums (in $kWhm^{-2}$) under all- and clear-sky conditions were estimated for all sites. To implement all the above calculations, a MatLab code was developed, which included the routine mXRONOS.

## 3. Results

### *3.1. Annual Solar Energy Potential*

Annual solar energy sums were derived from the database of each site by utilising the near-real ground albedo $\varrho_g$ in Equation (2). The annual solar energy sum (or yield) at each location was estimated by summing up all hourly solar radiation values within its TMY. Figure 3 shows the variation of the annual mean solar energy yields on a horizontal surface as well as on inclined flat-plate collectors mounted on a mode-(iii) solar tracker across all 43 sites and in the examined period; the diffuse solar radiation irradiation has been estimated by both transposition models of L-J and Hay. The difference in the average global solar irradiation value for the mode-(iii) system in comparison to that on a horizontal surface is: (i) with the L-J model ≈572 $kWhm^{-2}$ (or ≈33% increase) for all skies and ≈549 $kWhm^{-2}$ (or ≈37% increase) in clear-sky conditions, and (ii) with the Hay model ≈745 $kWhm^{-2}$ (or ≈43% increase) for all skies and ≈638 $kWhm^{-2}$ (or ≈43% increase) in clear-sky conditions. The above results show that the Hay model estimates higher global inclined irradiation in all cases of weather conditions than the L-J one. Nevertheless, real solar radiation measurements on mode-(iii) configuration solar trackers do not officially exist in Greece, so a comparison of the results of the present study to such measurements cannot be made. At first glance, these high differences imply a preference to use mode-(iii) solar systems instead of just horizontal solar collectors; this outcome would, however, be expected.

From Figure 3, one can see that $H_{g,t,L\text{-}J}$ varies between 2064 $kWhm^{-2}$ and 2709 $kWhm^{-2}$ [(average) 2298 $kWhm^{-2}$ ± (1σ) 133 $kWhm^{-2}$ = 2165 $kWhm^{-2}$ to 2431 $kWhm^{-2}$] for all skies and between 1743 $kWhm^{-2}$ and 2502 $kWhm^{-2}$ [(average) 2023 $kWhm^{-2}$ ± (1σ) 154 $kWhm^{-2}$ = 1869 $kWhm^{-2}$ to 2177 $kWhm^{-2}$] for

Preprints (www.preprints.org) | NOT PEER-REVIEWED | Posted: 8 May 2023 doi:10.20944/preprints202305.0488.v1

clear skies (σ = standard deviation); these values become for $H_{g,t,Hay}$ 2247 kWhm$^{-2}$ - 2878 kWhm$^{-2}$ [(average) 2471 kWhm$^{-2}$ ± (1σ) 127 kWhm$^{-2}$ = 2344 kWhm$^{-2}$ to 2598 kWhm$^{-2}$, all skies] and 1806 kWhm$^{-2}$ - 2617 kWhm$^{-2}$ [(average) 2113 kWhm$^{-2}$ ± (1σ) 156 kWhm$^{-2}$ = 1956 kWhm$^{-2}$ to 2269 kWhm$^{-2}$, for clear skies]. Figure 4 shows the above Hay-modelled findings in diagrammatic form. It is seen that the standard-deviation band is narrower in the all-sky case than in the clear-sky one, i.e., higher dispersion of the clear-sky $H_{g,t,Hay}$ values than the all-sky ones exists. This may be attributed to the selection process of those $H_{g,t,Hay}$ values that fall in the clear-sky zone (i.e., $0.65 < k'_t \leq 1$, Equation (11)); any such criterion like $k'_t$ cannot ensure 100% accuracy that the selected values of the variable will fully obey the criterion, but there may be other values of the variable that will falsely be classified in the clear-sky zone. Another observation from the graph in Figure 4 is that the out-of-the-±1σ-band solar irradiation values occur at higher latitudes, i.e., for $\varphi > 39^{o}$N. The explanation of this finding may be attributed to the higher weather variability in the northern part of Greece than the southern one, especially under clear skies. More specifically, under all-sky conditions 7 (or 16.3%) $H_{g,t,Hay}$ data points lie outside the ±1σ-band for $\varphi < 39^{o}$N and 8 (18.6%) for $\varphi > 39^{o}$N, while under clear-sky situations only 4 (9.3%) $H_{g,t,Hay}$ data points lie outside the ±1σ-band for $\varphi < 39^{o}$N and 9 (20.9%) for $\varphi > 39^{o}$N.

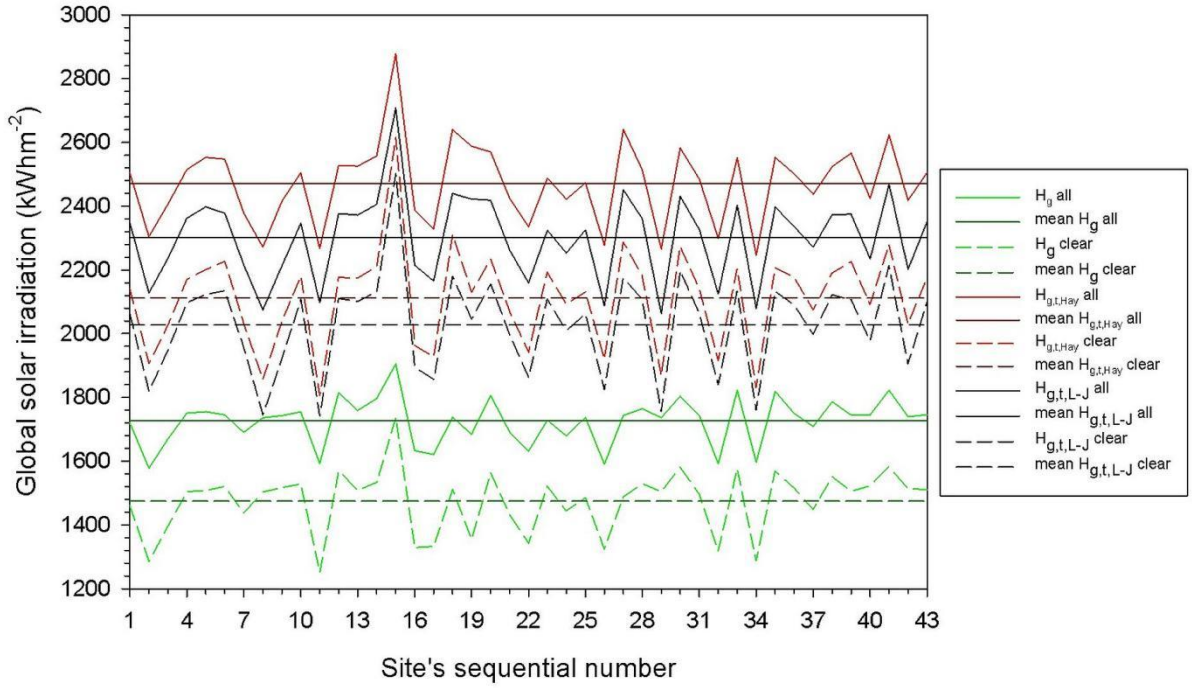


**Figure 3.** Variation of the annual mean solar energy yield across the 43 sites in Greece on horizontal surface (green lines), and on flat-plate surfaces fixed on mode-(iii) dynamic (red lines) systems estimated by both diffuse transposition models L-J and Hay. The solid lines represent the variation of the annual yields under all skies, while the short-dashed ones under clear-sky conditions. The horizontal straight lines show the average values all over the 43 sites and their TMYs.

Preprints (www.preprints.org) | NOT PEER-REVIEWED | Posted: 8 May 2023 doi:10.20944/preprints202305.0488.v1

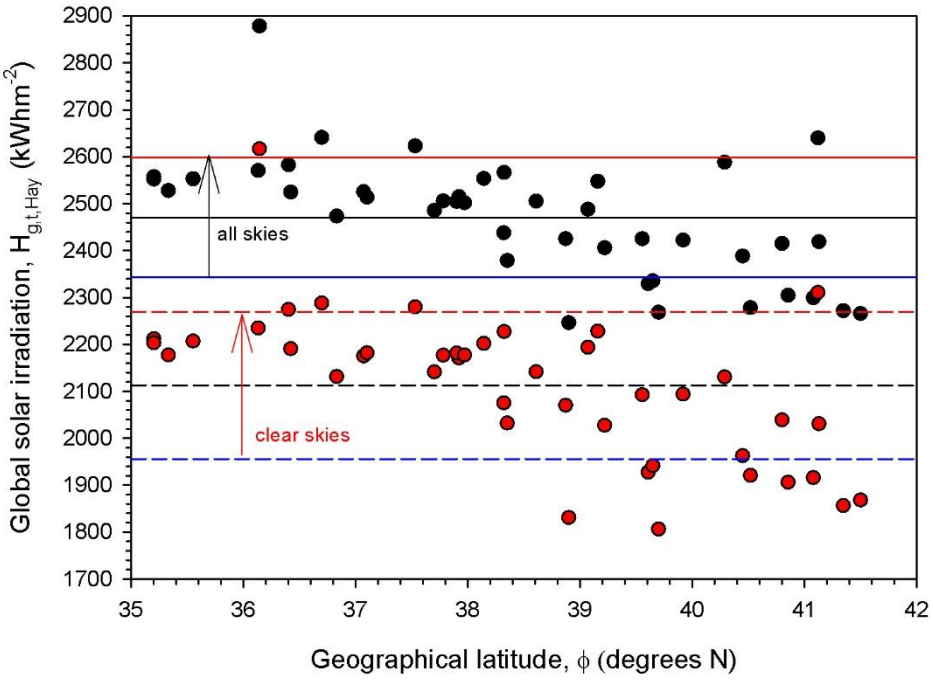


**Figure 4.** Variation of the annual mean solar energy yield, $H_{g,t,Hay}$, versus the geographical latitude, φ, across the 43 sites in Greece on flat-plate solar collectors fixed on mode-(iii) solar tracker under all- (black circles), and clear- (red circles) sky conditions over their TMYs. The black horizontal lines (solid for all and dashed for clear skies) show the annual averages. The arrows (black for all and red for clear skies) denote the ±1σ from the mean.

On the other hand, Kambezidis and Psiloglou [1], in their study about the solar energy efficiency of mode-(i) systems in Greece, have not reported an annual average global solar irradiation value; nevertheless, this average extracted from their Figure 6 results in ≈1875 kWhm$^{-2}$ under all-sky conditions (the authors used the L-J model with $\varrho_{g0}$ only); this gives a ≈9% increase with reference to the horizontal case and a ≈23% deficit in relation to mode-(iii) systems (present study with L-J model and $\varrho_g$). It should be noted here that their work was based on TMY data from 33 sites in Greece; the locations of the sites in that work coincide with the corresponding ones in the present 43-site study; for compatibility reasons, the locations of those 33 sites have been considered in the calculations of this issue. To make the results more documentary, Figure 5 shows the superiority of the mode-(iii) solar systems in terms of solar energy harvesting. Now, the differences are $H_{g,t,L\text{-}J/\varrho g} - H_{g,25\text{-}30S,L\text{-}J/\varrho g0} = 426.94$ kWhm$^{-2}$, $H_{g,t,L\text{-}J/\varrho g} - H_g = 582.22$ kWhm$^{-2}$, and $H_{g,25\text{-}30S,L\text{-}J/\varrho g0} - H_g = 155.29$ kWhm$^{-2}$. As seen in section 3.3, any of these 3 differences are comparable to or even double the monthly mean global solar irradiation for a mode-(iii) tracker across all 43 sites in Greece for all-sky conditions. This outcome gives another credit to investing in type-(iii) solar trackers because an extra month or two is gained by using it if maintenance costs are excluded. Farahat et al. [54] compared the 3 modes of solar harvesting in Saudi Arabia. They concluded that the Hay model must be preferred to the L-J one if a mode-(iii) tracking system is used for solar energy capture. Therefore, the rest of the calculations and analysis in the present work are done with the Hay model alone.

Working with the Hay transposition model only and near-real albedo values for the 33 sites in Greece, it is calculated that the annual solar energy potential on flat-plate solar collectors mounted on a dual-axis system is 81175 kWhm$^{-2}$ (all skies). This figure for 25°-30°-tilt flat-plate solar collectors toward the south (1875 kWhm$^{-2}$ per site x 33 sites) is 61875 kWhm$^{-2}$. The difference between these two figures is 19300 kWhm$^{-2}$; if this solar energy is divided by the annual solar energy per site (in our study 2460 kWhm$^{-2}$ = 81175 kWhm$^{-2}$ / 33 sites), it is concluded that a dual-axis system is 1.312 (= 2460 / 1875) times (or 31.2%) more efficient than the fixed-tilt system in Greece.

Preprints (www.preprints.org) | NOT PEER-REVIEWED | Posted: 8 May 2023 doi:10.20944/preprints202305.0488.v1

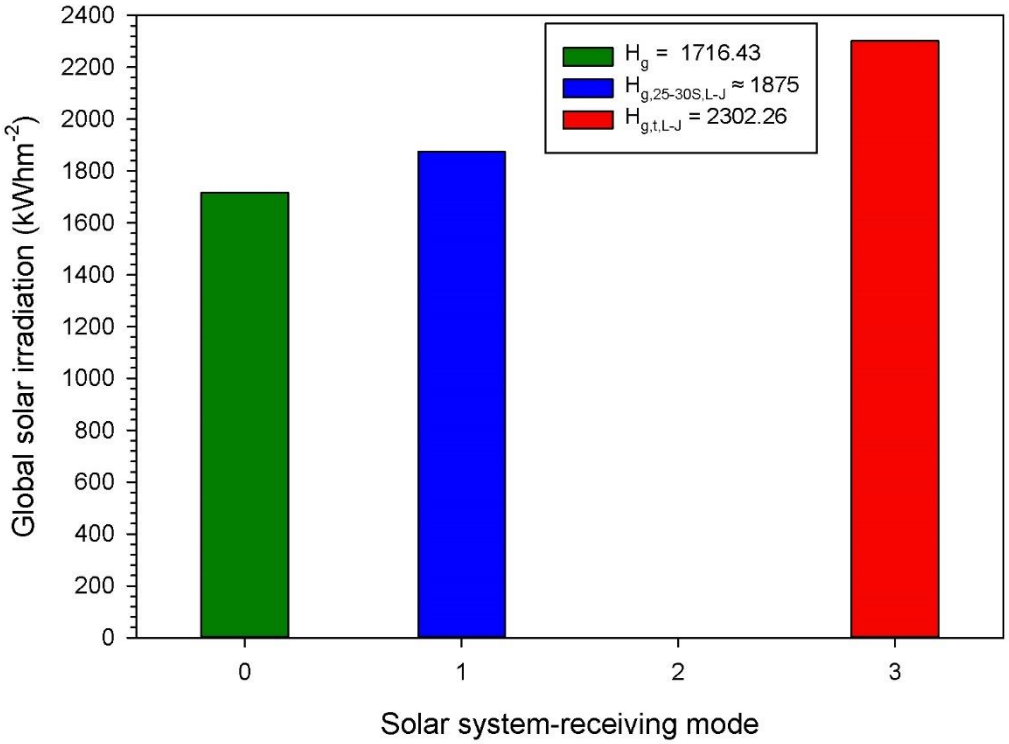


**Figure 5.** Annual mean solar energy yield across 33 sites in Greece for each type of installation; 0: horizontal surface; 1: mode-(i) static system (optimum tilt angles in the range 25° - 30° to south); 2: mode-(ii) dynamic system (optimum tilt angle tracking the Sun); 3: mode-(iii) dynamic system (varyin- tilt angle tracking the Sun); data for configuration mode-(ii) do not exist. The diffuse solar energy for mode-(i) and mode-(iii) systems has been estimated with the L-J model.

As a summary, Table 2 reports the total annual solar energy sum per site on flat-plate solar collectors mounted on a dual-axis solar tracker under all- and clear-sky conditions in Greece.

**Table 2. A**nnual solar energy sums for the 43 sites in Greece for flat-plate solar collectors mounted on mode-(iii) dynamic systems, $H_{g,t,Hay/\varrho g}$ under all- and clear-sky conditions within their TMYs. The $H_g$ values are rounded integers in kWhm$^{-2}$.

| Site number | $H_{g,t,Hay/\varrho g,all\ skies}$ | $H_{g,t,Hay/\varrho g,clear\ skies}$ |
|---|---|---|
| 1 | 2505 | 2141 |
| 2 | 2305 | 1906 |
| 3 | 2406 | 2027 |
| 4 | 2515 | 2171 |
| 5 | 2554 | 2202 |
| 6 | 2548 | 2228 |
| 7 | 2379 | 2032 |
| 8 | 2272 | 1856 |
| 9 | 2415 | 2039 |
| 10 | 2504 | 2181 |
| 11 | 2269 | 1806 |
| 12 | 2528 | 2177 |
| 13 | 2526 | 2175 |
| 14 | 2558 | 2211 |
| 15 | 2878 | 2617 |

Preprints (www.preprints.org) | NOT PEER-REVIEWED | Posted: 8 May 2023 doi:10.20944/preprints202305.0488.v1

| | | |
|---|---|---|
| 16 | 2388 | 1963 |
| 17 | 2330 | 1927 |
| 18 | 2640 | 2311 |
| 19 | 2588 | 2130 |
| 20 | 2571 | 2235 |
| 21 | 2425 | 2070 |
| 22 | 2336 | 1941 |
| 23 | 2488 | 2194 |
| 24 | 2422 | 2094 |
| 25 | 2473 | 2131 |
| 26 | 2278 | 1921 |
| 27 | 2641 | 2288 |
| 28 | 2514 | 2182 |
| 29 | 2266 | 1868 |
| 30 | 2583 | 2274 |
| 31 | 2486 | 2141 |
| 32 | 2299 | 1916 |
| 33 | 2552 | 2203 |
| 34 | 2247 | 1831 |
| 35 | 2553 | 2207 |
| 36 | 2502 | 2177 |
| 37 | 2438 | 2075 |
| 38 | 2525 | 2191 |
| 39 | 2567 | 2227 |
| 40 | 2425 | 2093 |
| 41 | 2623 | 2280 |
| 42 | 2419 | 2031 |
| 43 | 2506 | 2177 |
| **Sum** | **106245** | **90848** |
| **Average** | **2471** | **2113** |
| **Standard deviation (σ)** | **127** | **157** |
| **Average + 1σ** | **2598** | **2270** |
| **Average – 1σ** | **2344** | **1956** |

*3.2. Monthly Solar Energy Potential*

The intra-annual variation of $H_{g,t,Hay/Qg}$ for all sites is shown in Figures 6a, 6b. The variations of almost all sites are remarkably close, creating a bundle (band) under all- (Figure 6a) and clear- (Figure 6b) sky conditions. The amplitude of this band (i.e., dispersion of the monthly mean values) is ≈150 $Wm^{-2}$ in both cases. This can be confirmed by the comparable standard deviations of the average $H_{g,t,Hay/Qg}$ values for all- (127 $Wm^{-2}$) and clear- (157 $Wm^{-2}$) sky conditions (third line from bottom in Table 2).

From Figure 6, one can extract information about the solar energy yield per site and month. Nevertheless, this visual task is not very accurate for solar energy engineers and investors/entrepreneurs as they would like a guide to give them a more precise estimate of the monthly solar energy yield. For this reason, the monthly energy sums averaged over all sites and in their TMYs were estimated; their average intra-annual variation for all of Greece is shown in Figure 7. The same graphs show the ±1σ curves around the mean ones and the polynomial fits to the mean curves. It is easy to see that both mean, and polynomial-fit curves lie within the ±1σ band; this implies that there are no

Preprints (www.preprints.org) | NOT PEER-REVIEWED | Posted: 8 May 2023 doi:10.20944/preprints202305.0488.v1

abnormal (out fliers) monthly values that would result in drifting the mean and/or the fitted lines outside the ±1σ bands at all or certain months. Moreover, peak $H_{g,t,Hay/\varrho g}$ values occur in July (Figures 6 and 7), as anticipated. This is so because Greece is a country not close to the Equator; on the contrary, countries closer to the Equator provide a different intra-annual solar energy potential with higher values in spring and autumn than in summer, e.g. [55]; this is due to the solar paths (solar analemmas [56,57]) over such locations in a year-round. From Figure 7, the best-fit curves to the mean ones are 6th-order polynomials; their regression expressions are shown in Table 3. This order of polynomials has been selected as providing the highest $R^2$.

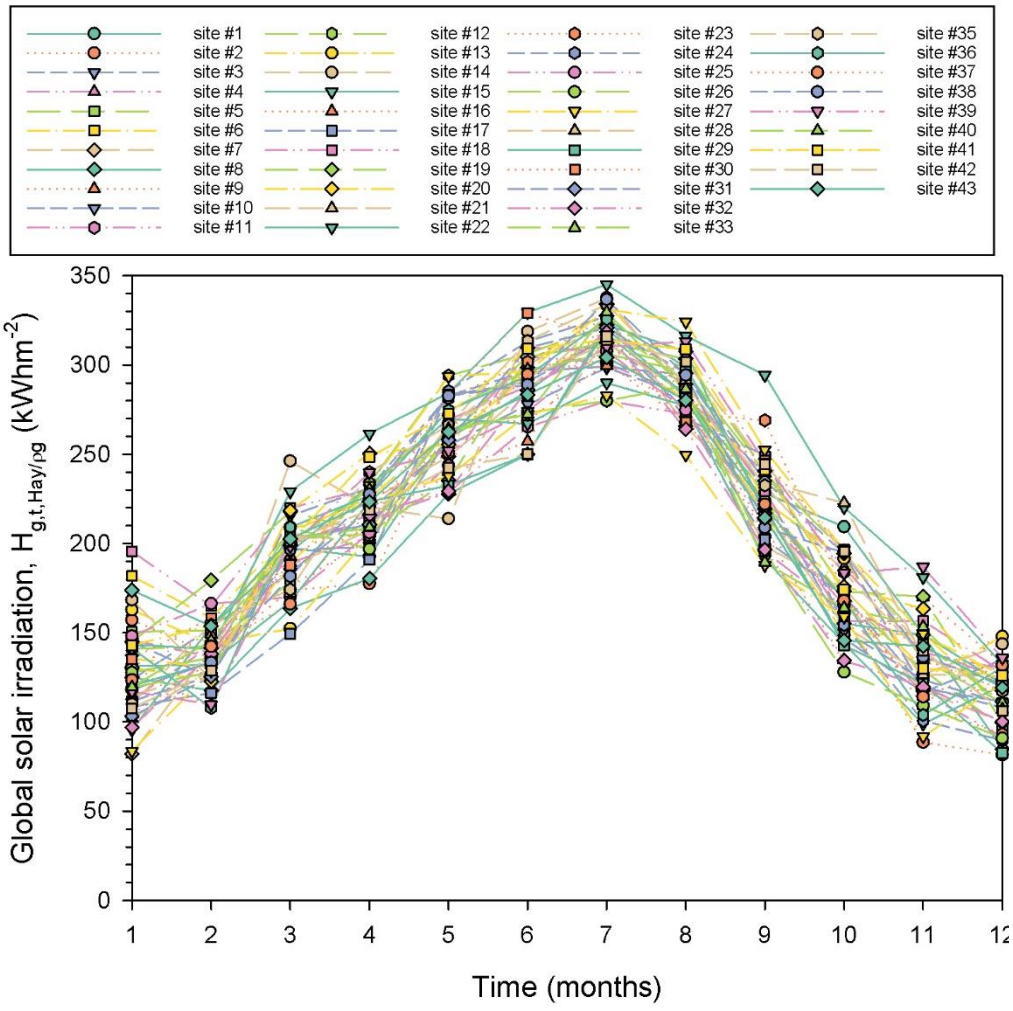


**(a)**

Preprints (www.preprints.org) | NOT PEER-REVIEWED | Posted: 8 May 2023 doi:10.20944/preprints202305.0488.v1

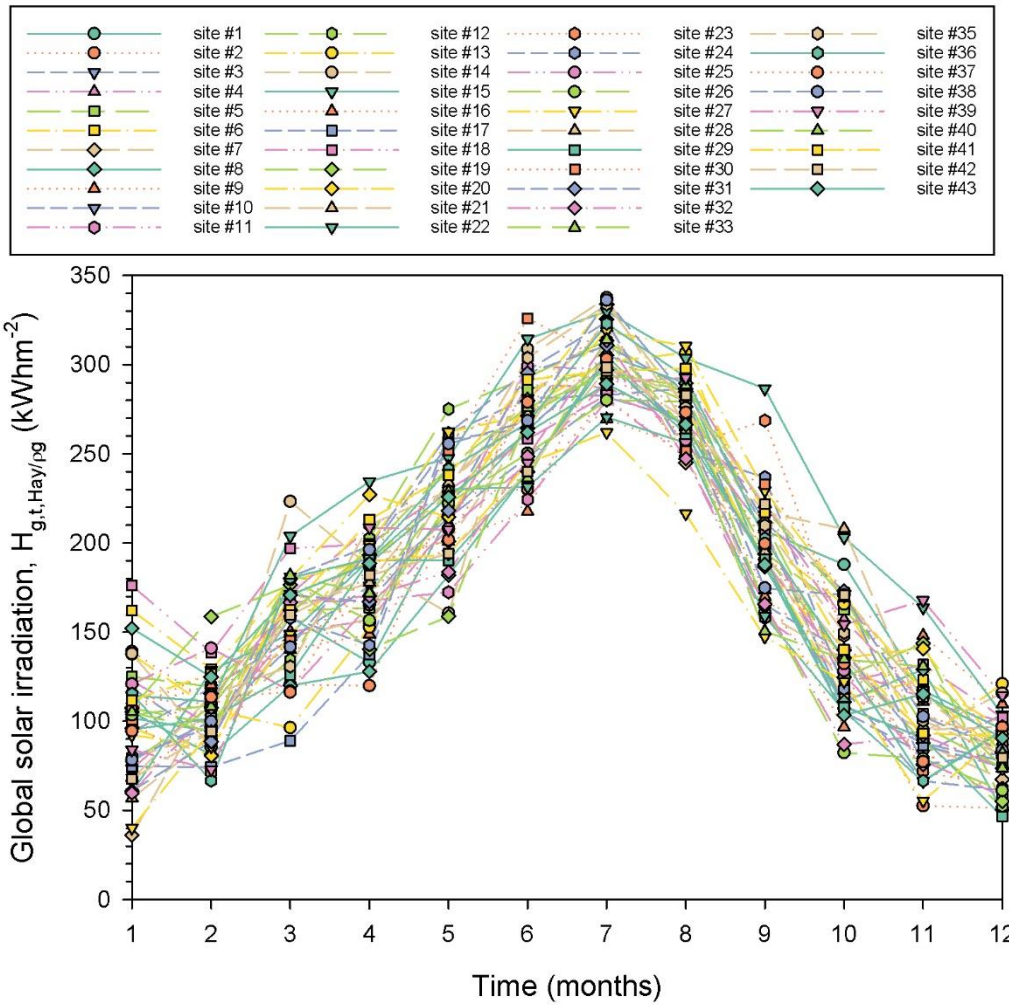


**(b)**

**Figure 6.** Monthly mean $H_{g,t,Hay/\rho g}$ variation under **(a)** all-, and **(b)** clear-sky conditions for all 43 sites in Greece. The monthly values are sums of the hourly solar radiation ones for each site. The numbers in the legend correspond to the sites shown in column 1, Table 1.

Preprints (www.preprints.org) | NOT PEER-REVIEWED | Posted: 8 May 2023 doi:10.20944/preprints202305.0488.v1

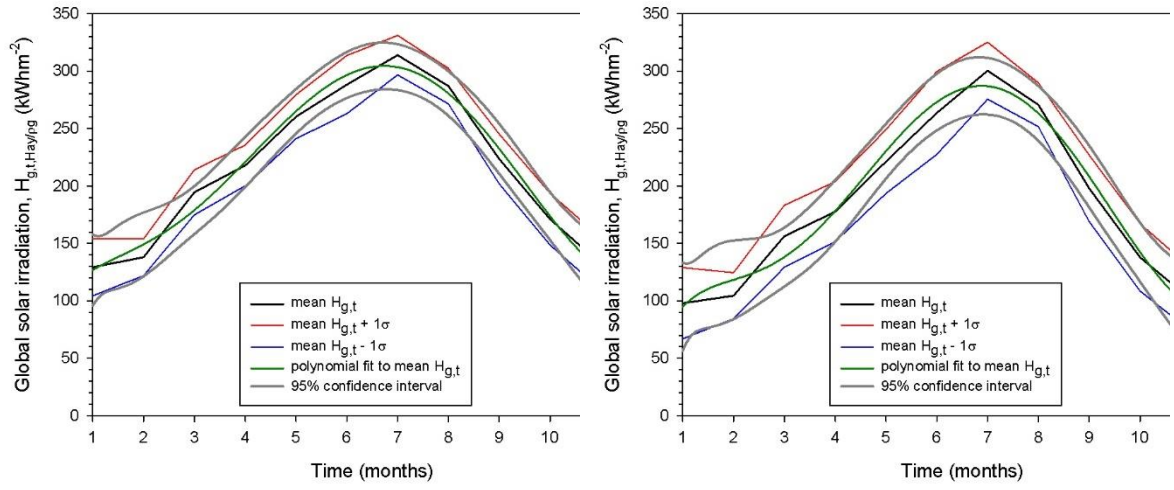


**Figure 7.** Intra-annual variation of $H_{g,t,Hay/\varrho g}$ under **(a)** all-, and **(b)** clear-sky conditions, averaged over all sites in Greece and over each month in their TMYs. The black solid line represents the average monthly $H_{g,t,Hay/\varrho g}$ sums. The red lines correspond to the mean $H_{g,t,Hay/\varrho g}$ + 1σ curves, and the blue lines to the mean $H_{g,t,Hay/\varrho g}$ – 1σ ones. The green lines refer to the best-fit curves to the mean $H_{g,t,Hay/\varrho g}$ ones. The grey lines denote the 95% confidence interval.

**Table 3.** Regression equations for the best-fit curves to the monthly and seasonal mean $H_{g,t,Hay/\varrho g}$ sums averaged over all 43 sites in Greece and over their TMYs, together with their $R^2$ values; t is either month in the range 1 - 12 (1 = January,…,12 = December) or season in the range 1 - 4 (1 = spring, …, 4 = winter). The regression equations are given for all- and clear-sky conditions. $R^2$ is the coefficient of determination.

| $R^2$ | Regression equation | Time scale, sky conditions |
|---|---|---|
| 0.9863<br>1 | $H_{g,t,Hay/\varrho g} = -0.0033t^6 + 0.1485t^5 - 2.3671t^4 + 15.9147t^3 - 44.9313t^2 + 76.8700t + 81.1407$<br>$H_{g,t,Hay/\varrho g} = -917.6945t^3 + 2542.8111t^2 - 1084.9270t + 132.6128$ | months, all<br>seasons, all |
| 0.9818<br>1 | $H_{g,t,Hay/\varrho g} = -0.0072t^6 + 0.3158t^5 - 5.0788t^4 + 36.7942t^3 - 121.8914t^2 + 198.4854t - 13.8347$<br>$H_{g,t,Hay/\varrho g} = -1325.2487t^3 + 2988.9232t^2 - 1262.3960t + 153.9639$ | months, clear<br>seasons, clear |

*3.3. Seasonal Solar Energy Potential*

In the northern hemisphere, the minimum and maximum energies received by solar-receiving systems occur during winter and summer, respectively. Therefore, this section is devoted to analysing the seasonal solar energy potential during spring (March-April-May), summer (June-July-August), autumn (September-October-November), and winter (December-January-February). The seasonal energy values at each site have been calculated by summing up all hourly solar radiation values in each season and then averaged over their TMYs.

As in the case of the intra-annual variation of the $H_{g,t,Hay/\varrho g}$ levels, Figure 8 presents the seasonal variation of the solar energy potential across all sites in Greece, as done for the monthly values in Figure 6. As expected, the solar energy potential peaks during summertime for all sites. Exceptionally higher $H_{g,t,Hay/\varrho g}$ levels occur at the site of Kastellorizo (site #15 on the map of Greece in Figure 1, a site at the southeastern corner of the country). The high annual solar energy potential of Kastellorizo is shown in Figure 4 (the black and red dots at $\varphi = 36.14^{o}$N), and in Table 2 (site #15).

Preprints (www.preprints.org) | NOT PEER-REVIEWED | Posted: 8 May 2023 doi:10.20944/preprints202305.0488.v1

To find an overall expression for the received average seasonal energy sum in Greece, as done for the monthly case, the energy values for each season from all sites were averaged over their TMYs under all- and clear-sky conditions; Figure 9 presents the results. Table 3 gives the regression equations for the curves that best fit the mean seasonal values. The fit is ideal ($R^2 = 1$).

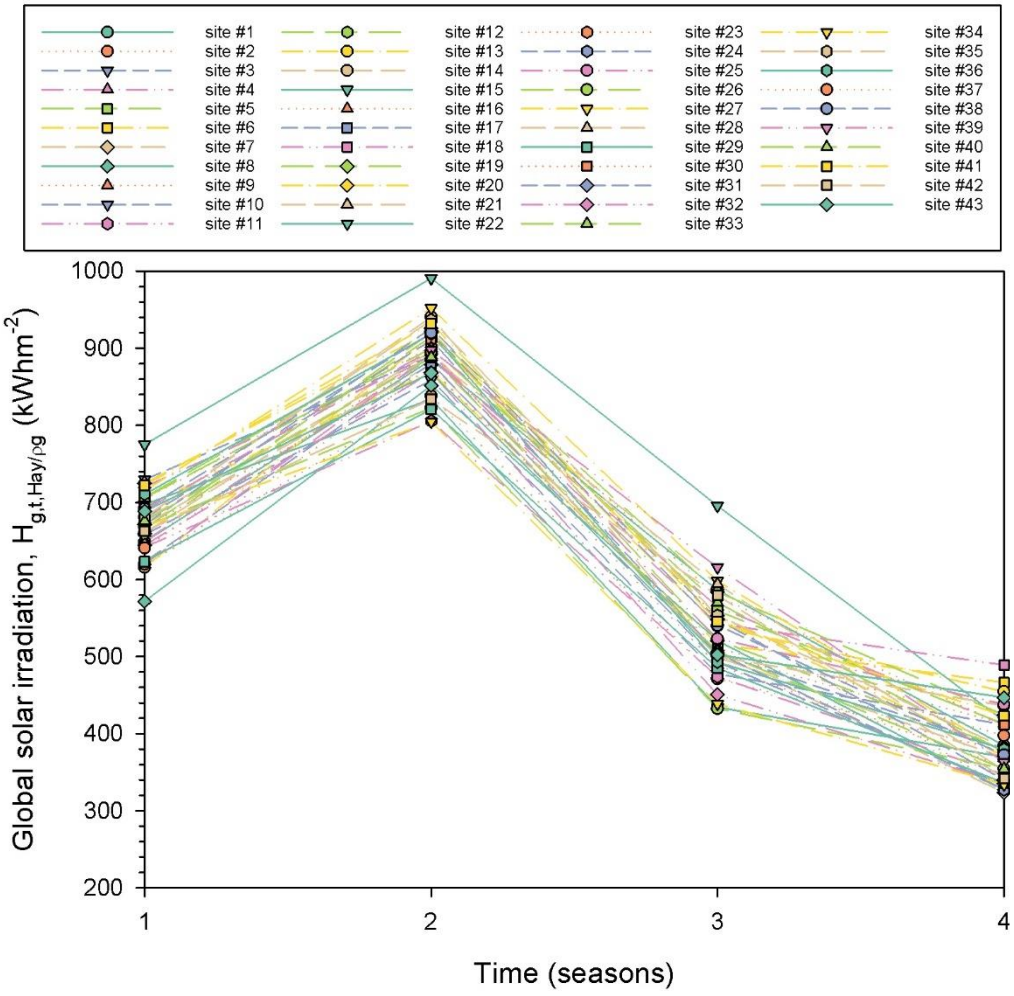


**(a)**

Preprints (www.preprints.org) | NOT PEER-REVIEWED | Posted: 8 May 2023 doi:10.20944/preprints202305.0488.v1

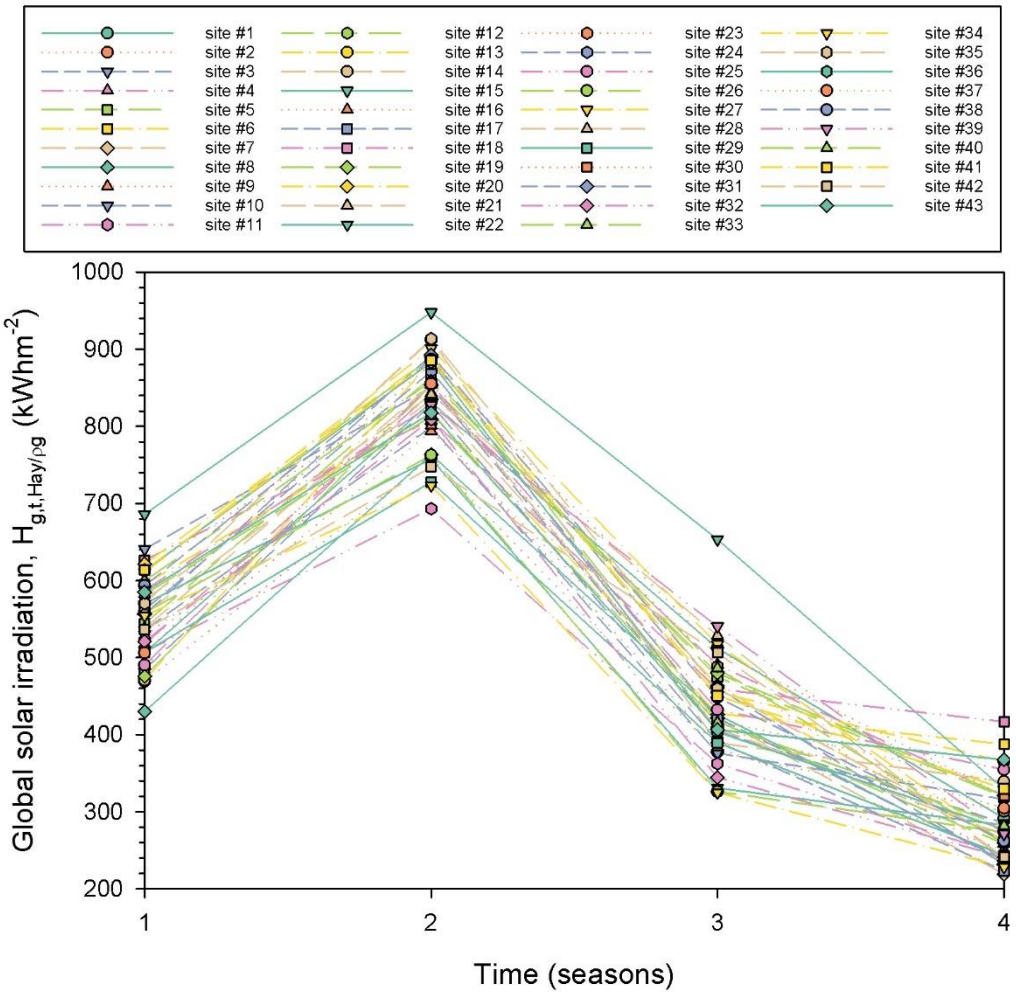


**(b)**

**Figure 8.** Seasonal mean $H_{g,t,Hay/og}$ variation under **(a)** all-, and **(b)** clear-sky conditions for all 43 sites in Greece. The seasonal values are sums of the hourly solar radiation ones for each site. The numbers in the legend correspond to the sites shown in column 1, Table 1. The numbers 1 - 4 in the *x*-axis refer to the seasons in the sequence 1 = spring to 4 = winter.

Preprints (www.preprints.org) | NOT PEER-REVIEWED | Posted: 8 May 2023 doi:10.20944/preprints202305.0488.v1

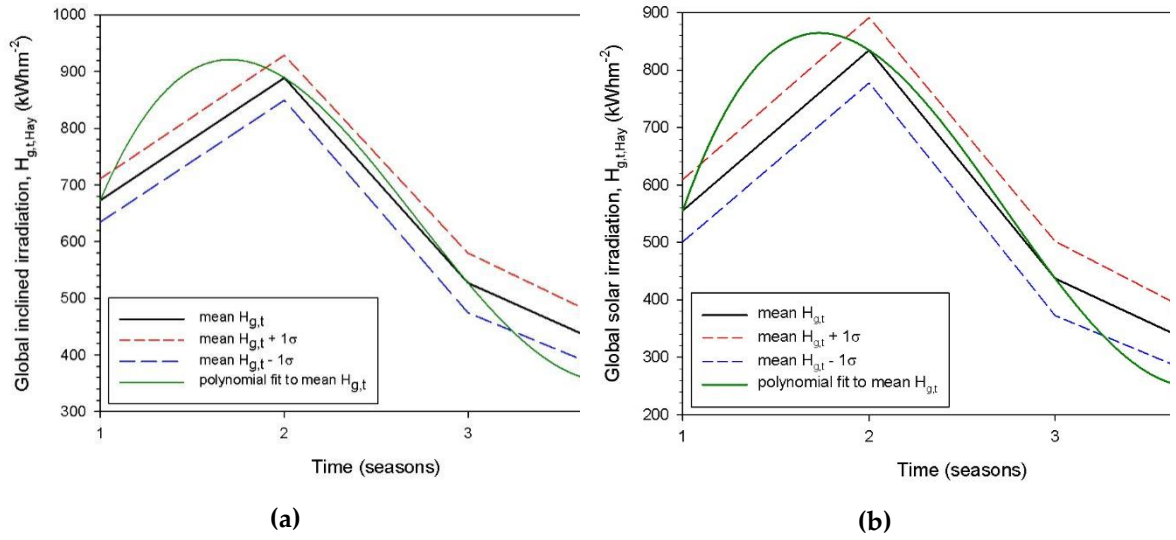


**Figure 9.** Seasonal variation of $H_{g,t,Hay/Qg}$ in Greece. The black lines represent the seasonal means. The red dashed lines refer to the mean $H_{g,t,Hay/Qg}$ + 1σ curves, and the blue dashed ones to the mean $H_{g,t,Hay/Qg}$ – 1σ curves, under **(a)** all-, and **(b)** clear-sky conditions. The $H_{g,t,Hay/Qg}$ values have been averaged over all 43 sites, and over each season in their TMYs. The green lines refer to the best-fit curves to the mean ones. The numbers 1 – 4 in the *x*-axis refer to the seasons in the sequence 1 = spring to 4 = winter.

### *3.4. Maps of Annual Solar Energy Potential*

Figure 10 shows the solar energy potential over Greece regarding the annual $H_{g,t,Hay/Qg}$ sums. A gradual increase in the annual solar energy potential in the direction N-S for both all- (Figure 10a) and clear- (Figure 10b) sky conditions is observed. Such a trend was found for the solar horizontal irradiances in Greece (see Figure 10b in [14]) as well as for the solar radiation received on flat-plate collectors inclined to the south at 25° - 30° (see Figure 11a in [1]). From the present Figures 10a and 10b, it is easy to realise that, in both cases, an (imaginary) horizontal line at φ ≈ 39°N divides the country into a northern part with lower solar energy availability and a southern one with higher $H_{g,t,Hay/Qg}$ levels. As confirmation, this was the outcome of a study about the solar radiation climate of Greece [14] in which the dividing line was also placed at φ = 39°N. Amazingly, the $H_{g,t,Hay/Qg}$ patterns in Figures 10a and 10b are almost identical. The interpretation of this remarkable similarity is attributed to two reasons. (i) Latitude: the higher the latitude, the lower the solar radiation levels received on the surface of the Earth and consequently on inclined flat-plate surfaces. (ii) Meteorology: more frequent cloudiness is observed in the northern part of the country; indeed, a relevant study for the cloudiness over the Mediterranean region shows a similar pattern over Greece on an annual basis to that in our Figure 10a (cf. Figure 1i in [58]).

Preprints (www.preprints.org) | NOT PEER-REVIEWED | Posted: 8 May 2023 doi:10.20944/preprints202305.0488.v1

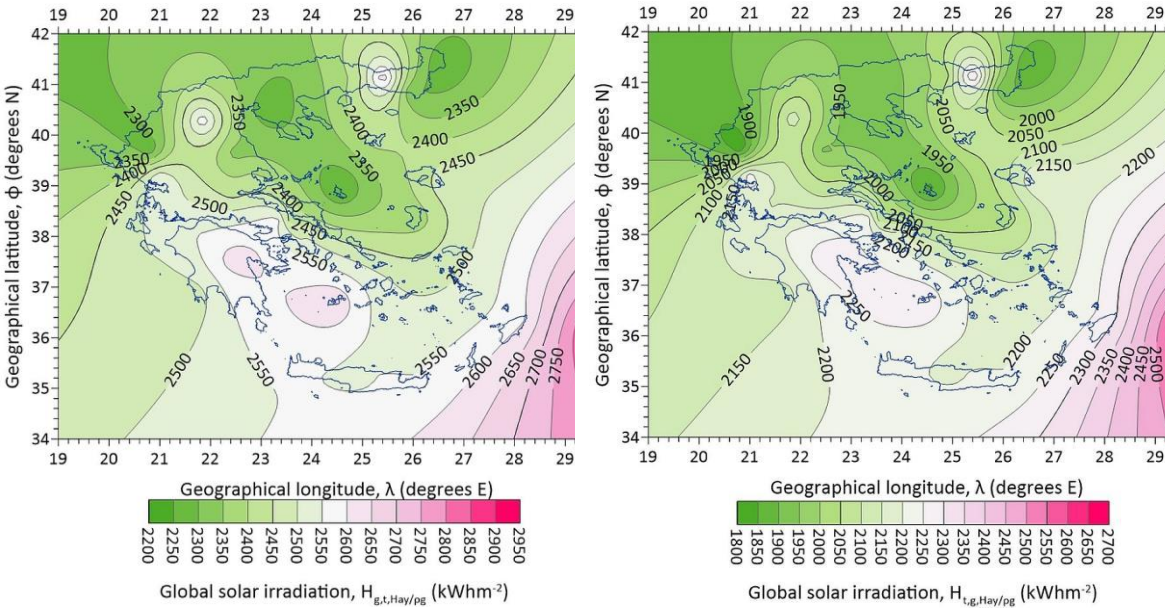


**(a)** **(b)**

**Figure 10.** Distribution of the annual $H_{g,t,Hay/\varrho g}$ sums across Greece, averaged over their TMYs; **(a)** all-, and **(b)** clear-sky conditions. The kriging geospatial interpolation method has been used to draw the isolines from the available 43 values.

### *3.5. Specialised Analysis*

This section is devoted to specific issues not belonging to the previous results. The topics to be tackled are the following: (i) accuracy of the PV-GIS simulations and variation of $H_{g,t,Hay/\varrho g}$ versus $H_{g,t,L\text{-}J/\varrho g}$ for all- and clear-sky conditions; (ii) effect of the $k_e$ index on solar harvesting ($H_{g,t,Hay/\varrho g}$); (iii) seasonal and monthly variation of $k_e$; (iv) dependence of the annual $H_{g,t,Hay/\varrho g}$ values on φ, z or $\varrho_g$; (v) seasonal maps of $H_{g,t,Hay/\varrho g}$; (vi) 3D maps of the annual $H_{g,t,Hay/\varrho g}$ values versus φ and $\varrho_g$ , and (vii) intra-annual variation of $\varrho_g$. All these issues are examined under all-sky conditions except for (i).

Various researchers [33,34,59,60,61] have shown that the PV-GIS tool simulates values for solar horizontal radiation with an accuracy between –14% to +11%, i.e., a median value of –1.5% very comparable to the ±3% accuracy of most pyranometers. That was done by comparing PV-GIS-simulated solar radiation values with real measurements. Therefore, no new evaluation is needed here for the PV-GIS tool. As far as the inter-dependence of the $H_{g,t,Hay/\varrho g}$ and $H_{g,t,L\text{-}J/\varrho g}$ estimated values is concerned, this is shown in Figure 11a for all- and Figure 11b for clear-sky conditions. In both cases, the inter-dependence is linear, as anticipated.

Preprints (www.preprints.org) | NOT PEER-REVIEWED | Posted: 8 May 2023 doi:10.20944/preprints202305.0488.v1

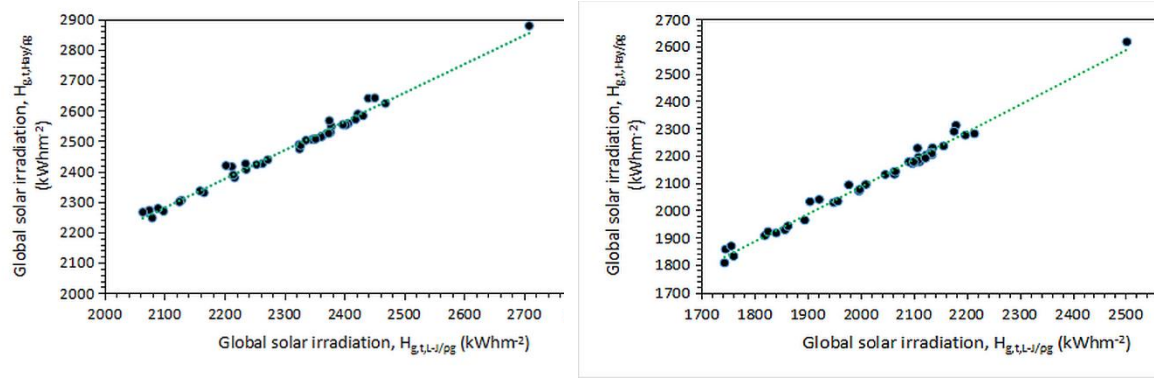


**Figure 11.** Inter-dependence of the annual mean $H_{g,t,Hay/\varrho g}$ and $H_{g,t,Hay/\varrho g}$ values for **(a)** all-, and **(b)** clear-sky conditions. The data points are averages over the TMY of each site. The linear fits to the data points have the following expressions: **(a)** $H_{g,t,Hay/\varrho g} = 0.9436H_{g,t,Hay/\varrho g} + 298.4800$ with $R^2 = 0.9848$, and **(b)** $H_{g,t,Hay/\varrho g} = 1.0017H_{g,t,Hay/\varrho g} + 81.5810$ with $R^2 = 0.9860$. The distant data points on the best-fit green dotted lines correspond to Kastellorizo (site #15 in Tables 1 and 2, and Figure 1).

Figure 12a shows the dependence of $H_{g,t,Hay/\varrho g}$ on $k_e$. A linear fit to the data points with a negative slope has been derived; this implies decreasing solar irradiation values with an increasing atmospheric extinction index. In other words, a 0.1 increase in $k_e$ results in an almost 1273 kWhm$^{-2}$ decrease in $H_{g,t,Hay/\varrho g}$, (calculated by applying the linear expression in Figure 12a twice for $k_{e1} = 0.38$ and $k_{e2} = 0.48$, computing the $H_{g,t,Hay/\varrho g1}$ and $H_{g,t,Hay/\varrho g2}$ values, and taking their difference ($H_{g,t,Hay/\varrho g2} - H_{g,t,Hay/\varrho g1}$)). As these energy values concern the whole Greek territory (i.e., the average value for all 43 sites), then a decrease of about 30 kWhm$^{-2}$ per site (= 1273 / 43) in a year-round is calculated or a decrease of ≈2.5 kWhm$^{-2}$ per site and per month (= 30 / 12). From Figure 7a, one sees that the average energy yield for January (worst case) is about 130 kWhm$^{-2}$ for all 43 sites or about 3.0 kWhm$^{-2}$ per site in January (= 130 / 43), and 330 kWhm$^{-2}$ in July (best case) for all 43 sites or 7.8 kWhm$^{-2}$ per site in July (= 330 / 43). The site-month values of 3.0 (7.8) kWhm$^{-2}$ are comparable (3 times higher) to the 2.5 kWhm$^{-2}$ decrease in $H_{g,t,Hay/\varrho g}$ due to a 0.1 increase in $k_e$. Since $k_e = H_d/H_b$ (consider $H_b$ = constant), a 0.1 increase in $k_e$ means a 10% increase in $H_d$, and a subsequent decrease in $H_{g,t,Hay/\varrho g}$ equal to 1273 kWhm$^{-2}$ (or 14% equivalently). Therefore, any solar energy investor in Greece should consult not only the solar energy potential map of Greece (Figure 10a), but also the corresponding map of $k_e$ in Figure 12b. In the latter map, higher $k_e$ values occur over the northern Aegean Sea, Macedonia, and Thrace regions, and lower ones over Peloponnese, Crete, and Rhodes. Taking into account a constant $H_b$ value concludes that favourable areas for solar harvesting in Greece are those of Peloponnese, Crete, and Rhodes because the contribution of the diffuse solar component is less important than in the northern areas; this way, no extra cost in the solar panels is anticipated in exploiting the higher diffuse radiation in northern Greece in respect to the $H_b$ component.

Preprints (www.preprints.org) | NOT PEER-REVIEWED | Posted: 8 May 2023 doi:10.20944/preprints202305.0488.v1

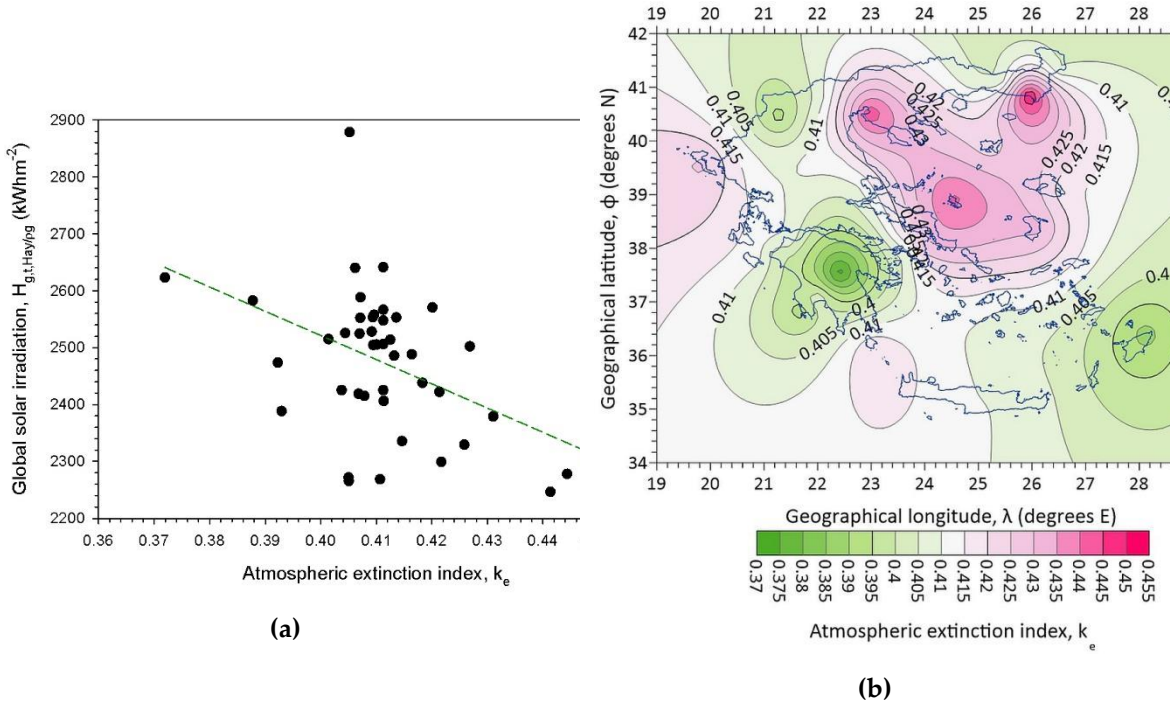


**Figure 12. (a)** Scatter plot of the annual mean data-point values of ($H_{g,t,Hay/\varrho g}$, $k_e$) over Greece under all-sky conditions, and averaged over their TMYs. The green dashed line is a linear fit to the data points with equation $H_{g,t,Hay/\varrho g}$, = –4256.9347$k_e$ + 4224.0925 and $R^2$ = 0.2148. **(b)** Map of the annual mean $k_e$ values under all-sky conditions across Greece and averaged over their TMYs. The kriging geospatial interpolation method has been used to draw the isolines from the available 43 values. The distant data point at $H_{g,t,Hay/\varrho g}$, ≈2900 kWhm$^{-2}$ in **(a)** corresponds to Kastellorizo (site #15 in Tables 1 and 2, and in Figure 1).

Now that the importance of the $k_e$ index in solar harvesting has been established, it is useful to derive and present the monthly and seasonal mean variation of the index for Greece. Figure 13 shows the intra-annual variation of $k_e$. It is interesting to observe that minimum values occur in the summertime due to lower $H_d/H_b$ values; this is so because, on the one hand, the $H_d$ levels are lower than in the other seasons (less frequent cloudiness), and, on the other hand, the $H_b$ levels are higher in this season. The above observations are also confirmed by Figure 14, which presents the seasonal variation of $k_e$ under all-sky conditions in Greece. The spring and summer $k_e$ patterns are remarkably similar; higher values in the northern part of Greece and lower in the south. The lower $k_e$ values imply lower diffuse radiation in comparison to the direct one; therefore, solar panels need to exploit the direct solar component without paying attention to the diffuse one in southern Greece; on the contrary, the diffuse radiation becomes more dominant in northern Greece, and this must be considered in PV installations. This outcome indicates a preference for solar harvesting below the latitude of φ ≈ 39°N (same conclusion in Section 3.4 for the annual values of $H_{g,t,Hay/\varrho g}$) during spring and summertime. On the contrary, the autumn and winter patterns differ; some relatively high values are spotted over the northern Aegean Sea, Macedonia, Thrace, and south of Peloponnese (autumn), and Crete, and almost all the Aegean Sea (winter). In these two seasons, the rule of an imaginary dividing line at φ ≈ 39°N is not obeyed.

Preprints (www.preprints.org) | NOT PEER-REVIEWED | Posted: 8 May 2023 doi:10.20944/preprints202305.0488.v1

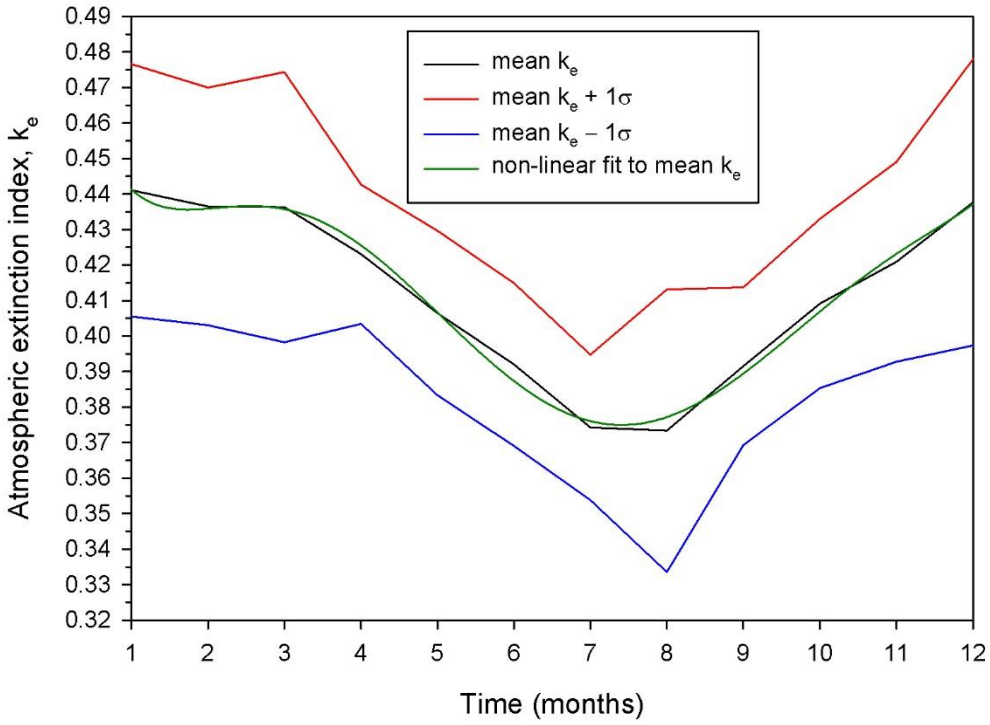


**Figure 13.** Intra-annual variation of $k_e$ over Greece under all-sky conditions. The values are averages over all 43 sites and in their TMYs. The black line presents the mean $k_e$ variation; the red line is the mean $k_e$ + 1σ curve; the blue line is the mean $k_e$ – 1σ curve; the green line shows the non-linear fitted curve to the mean $k_e$ one with equation $k_e = -1.1927t^6 - 823.7400t^5 - 26324.0000t^4 - 3x10^6t^3 - 4x10^7t^2 - 18x10^8t - 4x10^9$ and $R^2 = 0.9908$; t is month (1 for January, 12 for December).

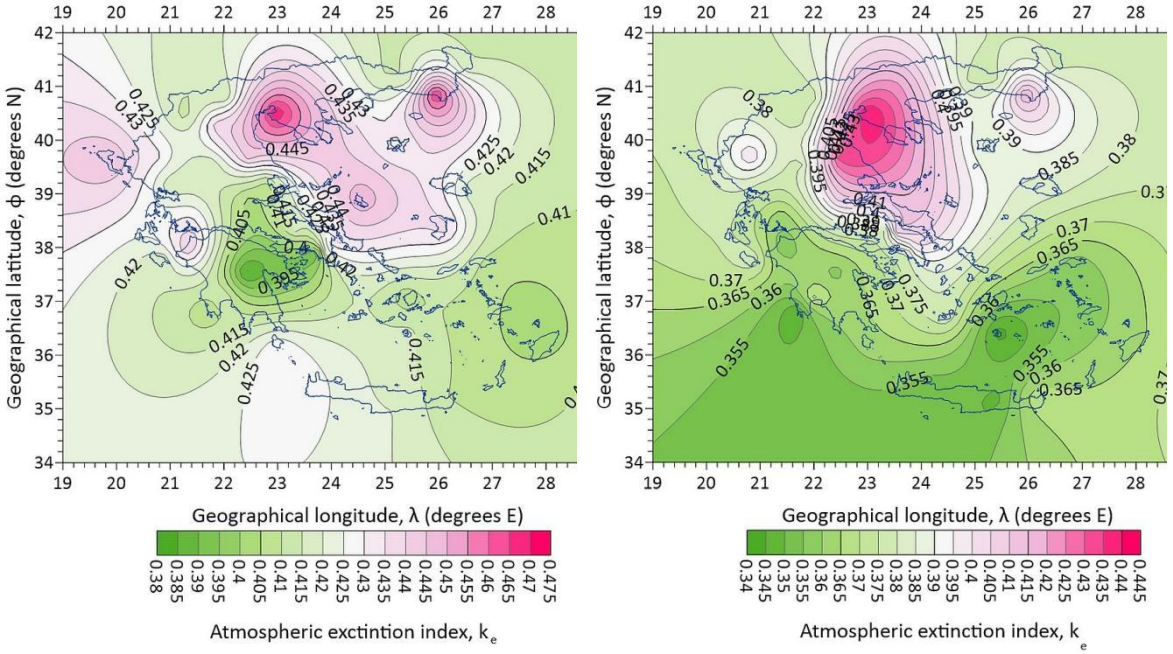


**(a)** **(b)**

Preprints (www.preprints.org) | NOT PEER-REVIEWED | Posted: 8 May 2023 doi:10.20944/preprints202305.0488.v1

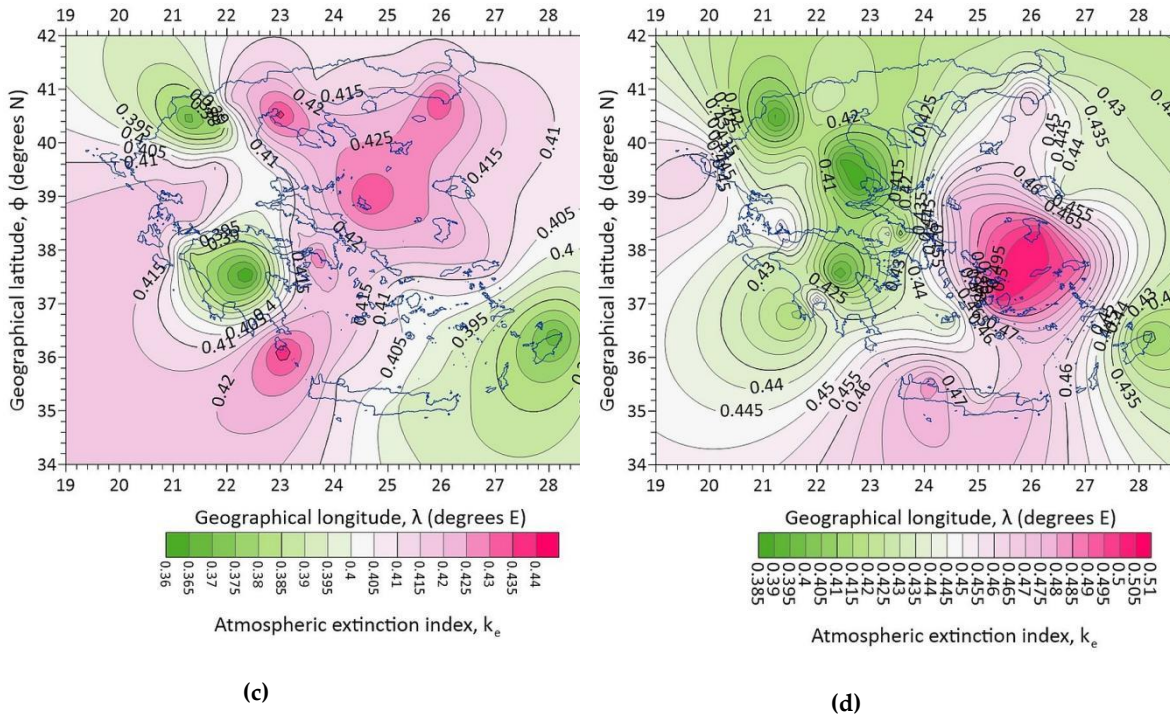


**Figure 14.** Maps of the atmospheric extinction index, $k_e$, over Greece under all-sky conditions, for **(a)** spring, **(b)** summer, **(c)** autumn, and **(d)** winter. The $k_e$ values are seasonal averages over their TMYs. The kriging geospatial interpolation method has been used to draw the isolines from the available 43 values.

The variation of the annual $H_{g,t,Hay/\varrho g}$ values versus φ is presented in Figure 4. Here, analogous plots are derived with respect to z or $\varrho_g$. Figure 15a shows the variation of the annual $H_{g,t,Hay/\varrho g}$ values versus z, and Figure 15b the variation of $H_{g,t,Hay/\varrho g}$ versus $\varrho_g$. In both Figures, a wide dispersion of the $H_{g,t,Hay}$ values versus z or $\varrho_g$ is seen; moreover, a lot of $H_{g,t,Hay}$ values occur at lower elevations (below 25 m amsl, vertical dashed line in Figure 15a) that shows that the global solar irradiation is not strictly related to the altitude of the site (at least in the range 0 m – 700 m amsl). Indeed, 16 sites out of 43 (37.2%) are at altitudes lower than 25 m amsl. Similar conclusion is drawn from Figure 15b; here the 6$^{th}$-order polynomial fit is shown to form two peaks at $\varrho_g \approx 0.116$ and $\approx 0.144$. The very loose dependence of the solar irradiation on flat-plate solar collectors fixed on dual-axis systems in Greece on either the site location (i.e., geographical latitude) or the type of ground (i.e., ground albedo) concludes that the general rule for a solar energy system installation is only the region (northern or southern Greece, see Figures 10 or 16).

Preprints (www.preprints.org) | NOT PEER-REVIEWED | Posted: 8 May 2023 doi:10.20944/preprints202305.0488.v1

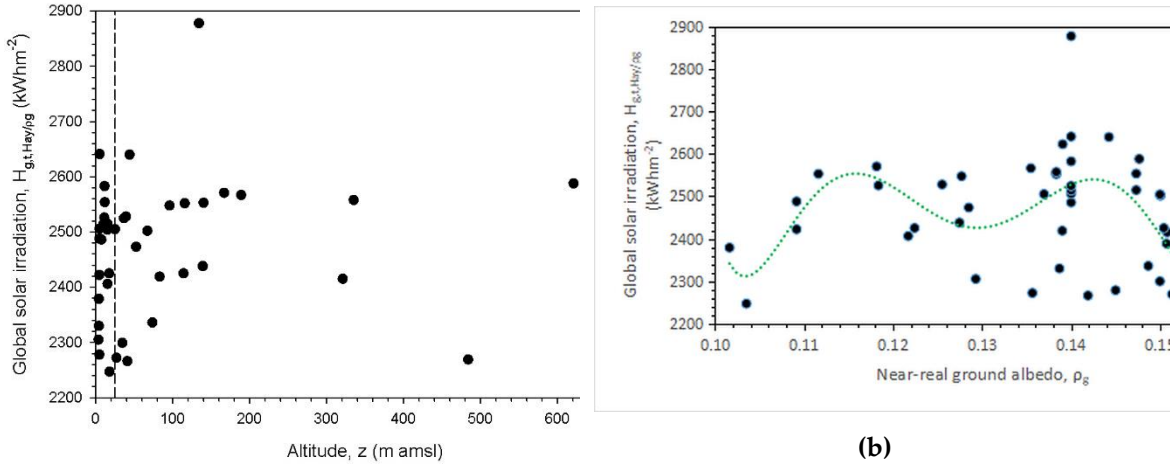


**(a)** **(b)**

**Figure 15. (a)** Scatter plot of the annual mean $H_{g,t,Hay/\varrho g}$ values as function of **(a)** the altitude, z (m amsl), and **(b)** the near-real ground albedo, $\varrho_g$, at the 43 sites in Greece under all-sky conditions, and averaged over their TMYs. The vertical black dashed line in **(a)** shows the altitude of z = 25 m amsl; the green dotted line in **(b)** is the best-fit curve to the ($H_{g,t,Hay/\varrho g}$, $\varrho_g$) data points with equation $H_{g,t,Hay/\varrho g} = 4x10^{12}\varrho_g^6 - 3x10^{12}\varrho_g^5 + 1x10^{12}\varrho_g^4 - 2x10^{11}\varrho_g^3 + 2x10^{10}\varrho_g^2 - 9x10^8\varrho_g + 2x10^7$ and $R^2 = 0.2224$ at a 95% confidence interval. The distant data point of $H_{g,t,Hay/\varrho g} \approx 2900$ kWhm$^{-2}$ in both graphs corresponds to Kastellorizo (site #15 in Tables 1 and 2, and in Figure 1).

Figure 16 presents the four seasonal maps of $H_{g,t,Hay/\varrho g}$ over Greece under all-sky conditions. It is easily seen that the $H_{g,t,Hay/\varrho g}$ patterns are the reverse of those for $k_e$ in the corresponding seasons. This is quite logical, because high global solar radiation consists mainly of direct solar component and less diffuse solar radiation; this is equivalent to low $k_e$ (i.e., $H_d/H_b$) values and vice versa.

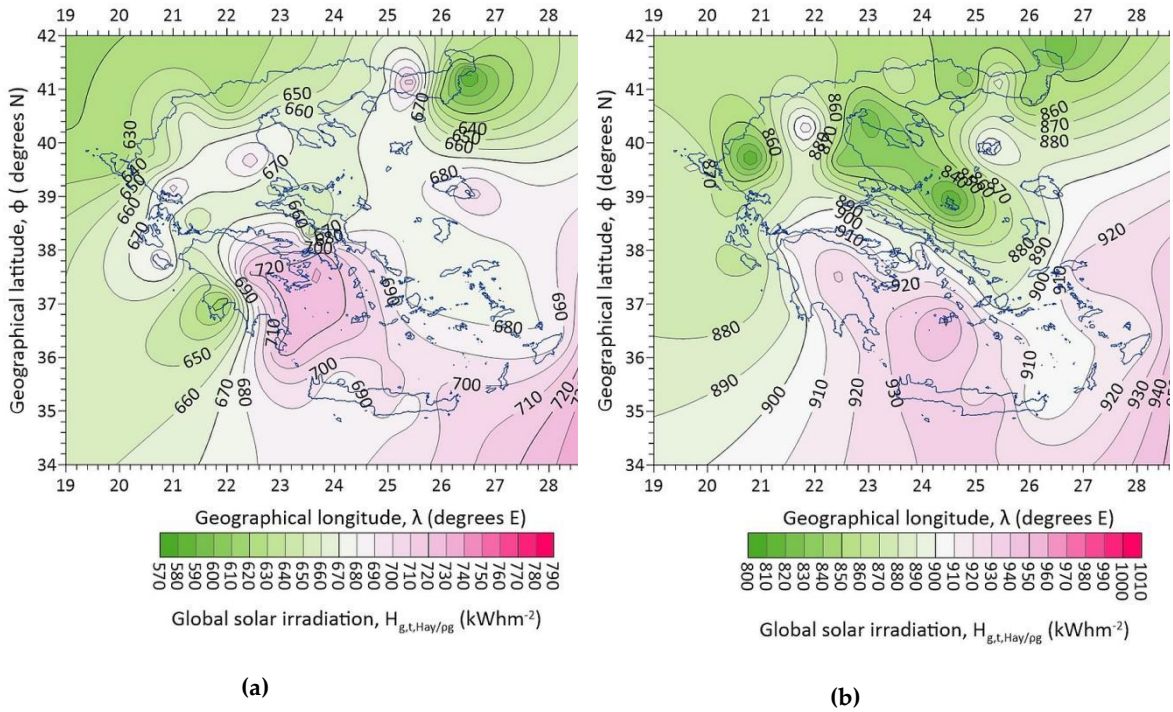


**(a)** **(b)**

Preprints (www.preprints.org) | NOT PEER-REVIEWED | Posted: 8 May 2023 doi:10.20944/preprints202305.0488.v1

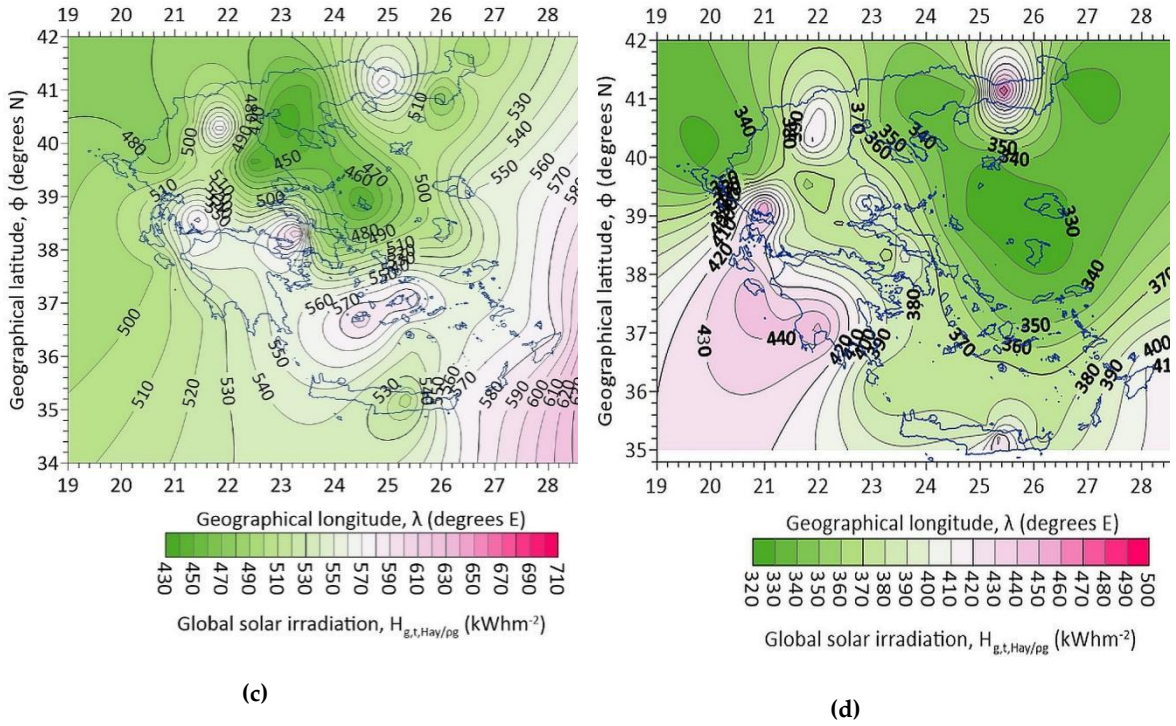


**Figure 16.** Maps of the global solar irradiation, $H_{g,t,Hay/\varrho g}$, over Greece under all-sky conditions, for **(a)** spring, **(b)** summer, **(c)** autumn, and **(d)** winter. All values are seasonal averages over their TMYs. The kriging geospatial interpolation method has been used to draw the isolines from the available 43 values.

Figure 17 presents a 3Dgraph of $H_{g,t,Hay/\varrho g}$ versus φ and $\varrho_g$ (Figure 17a), and a scatter plot of $\varrho_g$ versus φ (Figure 17b) under all-sky conditions. The $H_{g,t,Hay/\varrho g}$ pattern is a wave-like shape, confirmed by the 2D plot, in which the green line is a 6$^{th}$-order polynomial fit to the data points. This is an interesting result and shows that the reflections from the ground play a role in the performance of a dual-axis solar system. The big scatter in the data points of Figure 17b implies that the ground reflections do not depend directly on the geographical latitude; nevertheless, two peaks in the $\varrho_g$ values can be observed for φ ≈ 38°N and φ ≈ 41°N that correspond to sites located in central and northern Greece, where green lands (forests or cultivated areas) exist that reflect more radiation than the bare soil in most parts of the southern territories of the country (for φ < 38°N). Apart from the general territory rule of φ ≈ 39°N (see Figures 10 and 16) in investing solar energy systems in Greece that was formulated in (iv) above, one should also consider that a system installed at a site with φ = 38°N or φ = 41°N may receive almost 1.4 times higher ground reflection than other sites at φ ≈ 36°N or φ ≈ 39°N. On the other hand, a combination of Figures 15b and 17b results in Figure 17a, in which the solar irradiation levels over Greece take a waveform pattern.

Preprints (www.preprints.org) | NOT PEER-REVIEWED | Posted: 8 May 2023 doi:10.20944/preprints202305.0488.v1

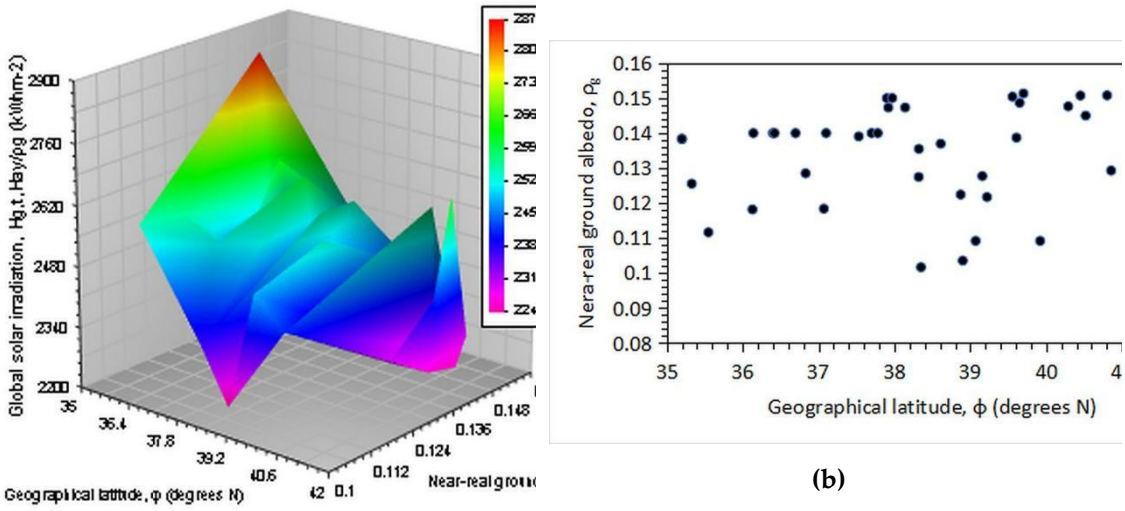


**Figure 17.** (a) 3D plot of $H_{g,t,Hay/\varrho g}$ versus φ and $\varrho_g$; (b) scatter plot of $\varrho_g$ versus φ. In both graphs the $H_{g,t,Hay/\varrho g}$ and $\varrho_g$ values are annual averages for each site in its TMY under all-sky conditions.

(vi) Figure 18 presents the intra-annual variation of the near-real ground albedo over Greece. The mean $\varrho_g \pm 1\sigma$ band is also shown and implies a $\varrho_g$ variation in the range of 0.108 - 0.155. This broad $\pm 1\sigma$ band is justified by the wide dispersion of the annual $\varrho_g$ values in relation to φ shown in Figure 17b. Nevertheless, an annual mean $\varrho_g$ value over Greece is estimated at 0.135. Psiloglou and Kambezidis [62] have estimated an annual ground-albedo value for Athens at 0.145 from solar radiation measurements at the Actinometric Station, National Observatory of Athens, Greece, in the period 1999 - 2008.

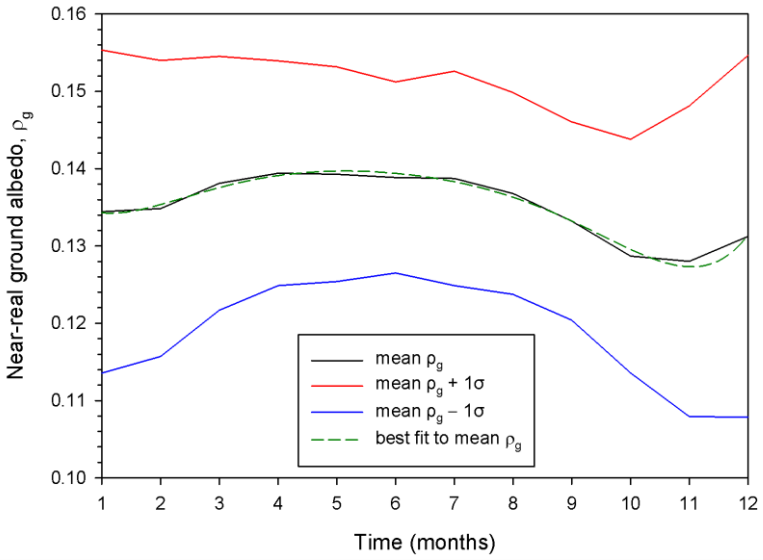


**Figure 18.** Intra-annual variation of the near-real ground albedo, $\varrho_g$; the monthly values are averages over all 43 sites and their TMYs under all-sky conditions. The black line shows the mean $\varrho_g$ curve, the red and blue lines the mean $\varrho_g + 1\sigma$ and mean $\varrho_g - 1\sigma$ curves, respectively; the green dashed line represents the best fit curve to the mean $\varrho_g$ one with equation $\varrho_g = -1.1927t^6 - 823.7400t^5 - 2.6324 \times 10^4 t^4 - 3 \times 10^6 t^3 - 4 \times 10^7 t^2 - 18 \times 10^8 \varrho_g - 2 \times 10^9$ with $R^2 = 0.9846$ at a 95% confidence interval; t is month (1 = January, …, 12 = December).

Preprints (www.preprints.org) | NOT PEER-REVIEWED | Posted: 8 May 2023 doi:10.20944/preprints202305.0488.v1

## 4. Discussion

This section refers to the discussion of related results found by other researchers.

Hammad et al. [63] compared the performance and cost between fixed-tilt (static) and double-axis (dynamic) systems in Jordan. They found 31.29% more energy produced by the 2-axis system in comparison with the static one, a figure quite comparable to our 31.2% (1.312 times) found in Section 3.1. Further, the authors estimated the payback period to be 27.6 months and 34.9 months for the dynamic and static systems, respectively, with corresponding electricity costs of 0.080 \$kWh$^{-1}$ and 0.100 \$kWh$^{-1}$.

Lazaroiu et al. [64] found a 12% - 20% increase in the energy produced by a dual-axis solar system in comparison to a fixed-tilt one in Romania, quite lower than our 31.2%.

Michaelides et al. [65] studied the performance of solar boilers for Athens, Greece, and Nicosia, Cyprus, by considering 1-axis, seasonal-tilt, and fixed-tilt systems. They found that the solar fractions (the normalised difference between the hot water energy provided by the Sun and the auxiliary one supplied by electricity) are 81.4%, 76.2%, and 74.4% for Athens, and 87.6%, 81.6%, and 79.7% for Nicosia in the case of a single-axis, a seasonal-tilt, and a fixed-tilt solar system, respectively.

As far as Saudi Arabia is concerned, Kambezidis et al. [66] found that mode-(iii) systems produce 4.22% more solar energy than mode-(ii) ones, 28.81% more solar energy than mode-(i) systems, and 37% in comparison to a flat-plate-receiving surface on horizontal plane. Their result of 28.81% is close to our 31.2%.

A study for the USA by Drury et al. [67] showed that mode-(ii) tracking systems can increase power generation by 12% - 25% in relation to fixed-tilt ones, and mode-(iii) tracking systems by 30% - 45%; the latter finding agrees marginally with our 31.2%. These researchers estimated the installation cost at 0.25 \$W$^{-1}$, 0.82 \$W$^{-1}$, and 1.23 \$W$^{-1}$ for fixed-tilt, 1-axis, and 2-axis systems, respectively. In the same way, their operation and maintenance costs were estimated at 25 \$kW$^{-1}$year$^{-1}$, 32 \$kW$^{-1}$year$^{-1}$, and 37.5 \$kW$^{-1}$year$^{-1}$, respectively.

Another study in Spain by Eke and Senturk [68] concluded that a double-axis solar system may result in an increase in electricity by 30.7% compared to a fixed-tilt one (a finding very close to our 31.2%).

Vaziri Rad et al. [69] in a study about the techno-economic and environmental features of different solar-tracking systems in Iran concluded that the dual-axis ones are the most efficient as they produce 32% more power on average compared to the fixed-tilt mode (a figure quite comparable to our 31.2%).

From the above discussion, one can easily conclude that the additional solar energy gain on solar panels fixed on mode-(iii) systems in comparison to mode-(i) ones depends on the terrain (surface albedo) surrounding the site in question and not on the absolute values of solar radiation received at the location. This is confirmed by the comparable figures of 31.29% in Jordan, 30.7% in Spain, and 32% in Iran to our 31.2%. On the contrary, the diverging figures of 12% - 20% in Romania, and 28.81% for Saudi Arabia may be attributed to the different landscape morphology in these cases to that of Greece. Further confirmation for this conclusion may be demonstrated by the wide range of solar energy gain within the USA (30% - 45%) due to the high variety in the surface morphology (deserts, high mountains, coastal regions, plains); nevertheless, the range of solar energy gain includes 31.2% (equal to ours), implying that this result has been extracted for locations with similar terrain to the Greek territory.

## 5. Conclusions

The present study investigated the solar energy potential across Greece on flat-plate solar panels that vary their tilt angle to receive solar radiation normally to their surfaces during the day. The main objective was to find the annual energy available in this configuration type under all- and clear-sky conditions. This was achieved by calculating the annual energy sum on flat-plate surfaces with varying tilt angles that track the Sun across Greece; the solar availability on a horizontal plane was also included for reference purposes. For this reason, hourly solar radiation data in typical meteorological years derived from 2005 to 2016 were downloaded from the PV-GIS platform for 43 sites of Greece.

Preprints (www.preprints.org) | NOT PEER-REVIEWED | Posted: 8 May 2023 doi:10.20944/preprints202305.0488.v1

The energy received on the tilted surfaces was calculated for near-real ground-albedo values downloaded from the Giovanni website.

The main result of the work was that the annual solar energy received by such (dynamic) mode-(iii) systems varies between 2247 $kWhm^{-2}$ and 2878 $kWhm^{-2}$ for all skies and between 1806 $kWhm^{-2}$ and 2617 $kWhm^{-2}$ under clear-sky conditions across Greece. These values have been calculated by using the HAY model. For the case of the L-J model, the above numbers become 2064 $kWhm^{-2}$ - 2709 $kWhm^{-2}$ for all- and 1743 $kWhm^{-2}$ - 2502 $kWhm^{-2}$ for clear-sky conditions. As reference, the corresponding values on the horizontal plane are 1726 $kWhm^{-2}$ and 1474 $kWhm^{-2}$. It was found that flat-plate solar panels mounted on a dual-axis tracking system provide 1.3 times higher energy than a fixed-tilt (mode-(i)) system in Greece. The distinction in clear skies was achieved by incorporating the modified clearness index, $k'_t$, in the calculations. In the rest of the analysis, only the HAY model was used by incorporating near-real ground-albedo values, $\varrho_g$.

The annual solar energy sums, and the monthly solar energy values averaged over all locations, and their corresponding TMYs were estimated under all-sky conditions. A regression equation was provided as a best-fit curve to the monthly mean solar energy sums that can estimate the solar energy potential at any location in Greece with great accuracy ($R^2 > 0.98$). This expression may prove especially useful to architects, civil engineers, solar energy engineers, and solar energy systems investors to assess the solar energy availability in Greece for solar-tracking flat-plate solar systems throughout the year.

Seasonal solar energy sums were also calculated. They were averaged over all sites and their TMYs under all-sky conditions. A new regression curve that best fits the mean values was estimated with absolute accuracy ($R^2 = 1$). Maximum sums were found in the summer (527 $kWm^{-2}$) and minimum ones in the winter (382 $kWm^{-2}$), as expected.

Though unified curves have been presented for the monthly and seasonal solar energy yields in all of Greece numerically expressed in Table 3, individual monthly and seasonal curves for all 43 sites were given in Figures 6 and 8, respectively, for the interested scientist or engineer to see the individual solar energy yield variation.

Annual maps of $H_{g,t,Hay/\varrho g}$ were derived from the annual mean solar energy sums of the 43 sites using the kriging geospatial interpolation method under all- and clear-sky conditions. In both cases, higher solar energy levels were found in southern Greece, a finding that may divide the country into two imaginary parts (northern and southern) at the latitude of $\varphi \approx 39^{o}$ N.

The atmospheric extinction index, $k_e$, was also used in the present study introduced by [52]. This index gives information about the contribution of the diffuse and direct solar radiation components in solar harvesting. A plot of the annual mean $H_{g,t,Hay/\varrho g}$ values versus $k_e$ showed a declining trend. Therefore, a map with annual mean $k_e$ values over Greece under all-sky conditions revealed an almost reverse pattern to that for $H_{g,t,Hay/\varrho g}$. Moreover, the intra-annual variation of the monthly mean $k_e$ values as well as seasonal maps of the atmospheric extinction index over Greece were derived. A best-fit curve was produced for the intra-annual variation. The seasonal $k_e$ maps showed patterns quite opposite to those for $H_{g,t,Hay/\varrho g}$, at least for spring and summer.

A 3D graph of $H_{g,t,Hay/\varrho g}$ versus $\varphi$ and $\varrho_g$ presented a waveform pattern. That was attributed to the combination of the variation in both independent parameters (see Figures 14a and 16a). The intra-annual variation of the ground albedo over Greece was also shown.

**Author Contributions:** Conceptualisation, methodology and original draft preparation, H.D.K.; data collection, data analysis, writing—review and editing, K.M.; writing—review and editing, K.A.K. All authors have read and agreed to the published version of the manuscript.

**Funding:** Not applicable.

**Institutional Review Board Statement:** Not applicable.

**Informed Consent Statement:** Not applicable.

**Data Availability Statement:** The solar radiation data and the ground-albedo ones for Greece are publicly available and were downloaded from the PV-GIS

 doi:10.20944/preprints202305.0488.v1

platform (https://ec.europa.eu/jrc/en/pvgis, accessed on 1 July 2020), and the Giovanni website (https://giovanni.gsfc.nasa.gov/giovanni/ accessed on 1 August 2020), respectively.

**Acknowledgments:** The authors are thankful to the Giovanni-platform staff, the MODIS-mission scientists, and associated NASA personnel for producing the ground-albedo data used in this research. They also thank the personnel of the PV-GIS platform for providing the necessary solar horizontal irradiances over Greece.

**Conflicts of Interest:** The authors declare no conflict of interest.

## References

(1) Kambezidis, H. D.; Psiloglou, B. E. Estimation of the Optimum Energy Received by Solar Energy Flat-Plate Convertors in Greece Using Typical Meteorological Years. Part I: South-Oriented Tilt Angles. *Applied Sciences (Switzerland)* **2021**, *11* (4), 1–27. https://doi.org/10.3390/app11041547.

(2) Demain, C.; Journée, M.; Bertrand, C. Evaluation of Different Models to Estimate the Global Solar Radiation on Inclined Surfaces. *Renew Energy* **2013**, *50*, 710–721. https://doi.org/10.1016/j.renene.2012.07.031.

(3) El-Sebaii, A. A.; Al-Hazmi, F. S.; Al-Ghamdi, A. A.; Yaghmour, S. J. Global, Direct and Diffuse Solar Radiation on Horizontal and Tilted Surfaces in Jeddah, Saudi Arabia. *Appl Energy* **2010**, *87* (2), 568–576. https://doi.org/10.1016/j.apenergy.2009.06.032.

(4) García, I.; de Blas, M.; Hernández, B.; Sáenz, C.; Torres, J. L. Diffuse Irradiance on Tilted Planes in Urban Environments: Evaluation of Models Modified with Sky and Circumsolar View Factors. *Renew Energy* **2021**, *180*, 1194–1209. https://doi.org/10.1016/j.renene.2021.08.042.

(5) Barbón, A.; Bayón, L.; Díaz, G.; Silva, C. A. Investigation of the Effect of Albedo in Photovoltaic Systems for Urban Applications: Case Study for Spain. *Energies (Basel)* **2022**, *15* (21), 7905. https://doi.org/10.3390/en15217905.

(6) Akbar, H. S.; Fathallah, M. N.; Raoof, O. O. Efficient Single Axis Sun Tracker Design for Photovoltaic System Applications. *IOSR Journal of Applied Physics* **2017**, *09* (02), 53–60. https://doi.org/10.9790/4861-0902025360.

(7) Heslop, S.; MacGill, I. Comparative Analysis of the Variability of Fixed and Tracking Photovoltaic Systems. *Solar Energy* **2014**, *107*, 351–364. https://doi.org/10.1016/j.solener.2014.05.015.

(8) Abdallah, S.; Nijmeh, S. Two Axes Sun Tracking System with PLC Control. *Energy Convers Manag* **2004**, *45* (11–12), 1931–1939. https://doi.org/10.1016/j.enconman.2003.10.007.

(9) Akbar, H. S. Design of Sun Tracker System for Solar Energy Applications. *Journal of Physics and Research (IJPR)* **2015**, *1* (1), 29–34.

(10) Hafez, A. Z.; Yousef, A. M.; Harag, N. M. Solar Tracking Systems: Technologies and Trackers Drive Types – A Review. *Renewable and Sustainable Energy Reviews* **2018**, *91* (November 2017), 754–782. https://doi.org/10.1016/j.rser.2018.03.094.

(11) Altarawneh, I. S.; Rawadieh, S. I.; Tarawneh, M. S.; Alrowwad, S. M.; Rimawi, F. Optimal Tilt Angle Trajectory for Maximizing Solar Energy Potential in Ma'an Area in Jordan. *Journal of Renewable and Sustainable Energy* **2016**, *8* (3). https://doi.org/10.1063/1.4948389.

(12) Talebizadeh, P.; Mehrabian, M. A.; Abdolzadeh, M. Prediction of the Optimum Slope and Surface Azimuth Angles Using the Genetic Algorithm. *Energy Build* **2011**, *43* (11), 2998–3005. https://doi.org/10.1016/j.enbuild.2011.07.013.

(13) Evseev, E. G.; Kudish, A. I. The Assessment of Different Models to Predict the Global Solar Radiation on a Surface Tilted to the South. *Solar Energy* **2009**, *83* (3), 377–388. https://doi.org/10.1016/j.solener.2008.08.010.

(14) Kambezidis, H. D. The Solar Radiation Climate of Greece. *Climate* **2021**, *9*, 183–202. https://doi.org/10.3390/cli9120183.

(15) Kaddoura, T. O.; Ramli, M. A. M.; Al-Turki, Y. A. On the Estimation of the Optimum Tilt Angle of PV Panel in Saudi Arabia. *Renewable and Sustainable Energy Reviews* **2016**, *65*, 626–634. https://doi.org/10.1016/j.rser.2016.07.032.

(16) Ohtake, H.; Uno, F.; Oozeki, T.; Yamada, Y.; Takenaka, H.; Nakajima, T. Y. Estimation of Satellite-Derived Regional Photovoltaic Power Generation Using a Satellite-Estimated Solar Radiation Data. *Energy Sci Eng* **2018**, *6* (5), 570–583. https://doi.org/10.1002/ese3.233.

(17) Tsalides, P.; Thanailakis, A. Direct Computation of the Array Optimum Tilt Angle in Constant-Tilt Photovoltaic Systems. *Solar Cells* **1985**, *14* (1), 83–94. https://doi.org/10.1016/0379-6787(85)90008-0.

(18) Koronakis, P. S. On the Choice of the Angle of Tilt for South Facing Solar Collectors in the Athens Basin Area. *Solar Energy* **1986**, *36* (3), 217–225. https://doi.org/10.1016/0038-092X(86)90137-4.

(19) Balouktsis, A.; Tsanakas, D.; Vachtevanos, G. On the Optimum Tilt Angle of a Photovoltaic Array. *International Journal of Solar Energy* **1987**, *5* (3), 153–169. https://doi.org/10.1080/01425918708914416.

(20) Synodinou, B. M.; Katsoulis, B. D. A Comparison of Three Models for Estimation of Global Solar Irradiation on Tilted and Oriented Surfaces in Athens. *International Journal of Solar Energy* **1996**, *18* (2), 83–102. https://doi.org/10.1080/01425919608914308.

(21) Darhmaoui, H.; Lahjouji, D. Latitude Based Model for Tilt Angle Optimization for Solar Collectors in the Mediterranean Region. In *Energy Procedia*; 2013; Vol. 42, pp 426–435. https://doi.org/10.1016/j.egypro.2013.11.043.

(22) Kaldellis, J. K.; Kapsali, M.; Kavadias, K. A. Temperature and Wind Speed Impact on the Efficiency of PV Installations. Experience Obtained from Outdoor Measurements in Greece. *Renew Energy* **2014**, *66*, 612–624. https://doi.org/10.1016/j.renene.2013.12.041.

(23) Jacobson, M. Z.; Jadhav, V. World Estimates of PV Optimal Tilt Angles and Ratios of Sunlight Incident upon Tilted and Tracked PV Panels Relative to Horizontal Panels. *Solar Energy* **2018**, *169* (April), 55–66. https://doi.org/10.1016/j.solener.2018.04.030.

(24) Raptis, I.-P.; Moustaka, A.; Kosmopoulos, P.; Kazadzis, S. Selecting Surface Inclination for Maximum Solar Power. *Energies (Basel)* **2022**, *15* (13), 4784. https://doi.org/10.3390/en15134784.

(25) Palz, W.; Greif, J. Introduction to the Tables for Daily Global and Diffuse Radiation Incident on Slopes. In *European Solar Radiation Atlas*; Palz, W., Greif, J., Eds.; Springer Berlin Heidelberg: Berlin, Heidelberg, 1996; pp 25–27. https://doi.org/10.1007/978-3-642-80237-9_17.

(26) Page, J.; Albuisson, M.; Wald, L. The European Solar Radiation Atlas: A Valuable Digital Tool. *Solar Energy* **2001**, *71* (1), 81–83. https://doi.org/10.1016/S0038-092X(00)00157-2.

(27) ESMAP. *Global Solar Atlas 2.0*; Washington, DC, 2019. www.solargis.com.

(28) Kambezidis, H. D.; Psiloglou, B. E.; Kavadias, K. A.; Paliatsos, A. G.; Bartzokas, A. Development of a Greek Solar Map Based on Solar Model Estimations. *Sun and Geosphere* **2016**, *11* (2), 137–141.

(29) Katopodis, T.; Markantonis, I.; Politi, N.; Vlachogiannis, D.; Sfetsos, A. High-Resolution Solar Climate Atlas for Greece under Climate Change Using the Weather Research and Forecasting (WRF) Model. *Atmosphere (Basel)* **2020**, *11* (7), 761. https://doi.org/10.3390/atmos11070761.

(30) Huld, T.; Müller, R.; Gambardella, A. A New Solar Radiation Database for Estimating PV Performance in Europe and Africa. *Solar Energy* **2012**, *86* (6), 1803–1815. https://doi.org/10.1016/j.solener.2012.03.006.

(31) Urraca, R.; Gracia-Amillo, A. M.; Koubli, E.; Huld, T.; Trentmann, J.; Riihelä, A.; Lindfors, A. V.; Palmer, D.; Gottschalg, R.; Antonanzas-Torres, F. Extensive Validation of CM SAF Surface Radiation Products over Europe. *Remote Sens Environ* **2017**, *199* (September), 171–186. https://doi.org/10.1016/j.rse.2017.07.013.

(32) Urraca, R.; Huld, T.; Gracia-Amillo, A.; Martinez-de-Pison, F. J.; Kaspar, F.; Sanz-Garcia, A. Evaluation of Global Horizontal Irradiance Estimates from ERA5 and COSMO-REA6 Reanalyses Using Ground and Satellite-Based Data. *Solar Energy* **2018**, *164* (October 2017), 339–354. https://doi.org/10.1016/j.solener.2018.02.059.

(33) Mueller, R. W.; Matsoukas, C.; Gratzki, A.; Behr, H. D.; Hollmann, R. The CM-SAF Operational Scheme for the Satellite Based Retrieval of Solar Surface Irradiance - A LUT Based Eigenvector Hybrid Approach. *Remote Sens Environ* **2009**, *113* (5), 1012–1024. https://doi.org/10.1016/j.rse.2009.01.012.

(34) Amillo, A. G.; Huld, T.; Müller, R. A New Database of Global and Direct Solar Radiation Using the Eastern Meteosat Satellite, Models and Validation. *Remote Sens (Basel)* **2014**, *6* (9), 8165–8189. https://doi.org/10.3390/rs6098165.
(35) Walraven, R. Calculating the Position of the Sun. *Solar Energy* **1978**, *20* (5), 393–397. https://doi.org/10.1016/0038-092X(78)90155-X.
(36) Wilkinson, B. J. An Improved FORTRAN Program for the Rapid Calculation of the Solar Position. *Solar Energy* **1981**, *27* (1), 67–68. https://doi.org/10.1016/0038-092X(81)90021-9.
(37) Kambezidis, H. D.; Papanikolaou, N. S. Solar Position and Atmospheric Refraction. *Solar Energy* **1990**, *44* (3), 143–144. https://doi.org/10.1016/0038-092X(90)90076-O.
(38) Kambezidis, H. D.; Mimidis, K.; Kavadias, K. A. Correction of the Solar Azimuth Discontinuity at Sunrise and Sunset. *Sun and Geosphere* **2022**, *15* (1), 19–34. https://doi.org/10.31401/SunGeo.2022.01.04.
(39) Liu, B.; Jordan, R. C. The Long-Term Average Performance of Flat-Plate Solar-Energy Collectors. *Solar Energy* **1963**, *7* (2), 53–74.
(40) Hay, J. E. Calculation of Monthly Mean Solar Radiation for Horizontal and Inclined Surfaces. *Solar Energy* **1979**, *23* (4), 301–307. https://doi.org/10.1016/0038-092X(79)90123-3.
(41) Hay, J. E. Calculating Solar Radiation for Inclined Surfaces: Practical Approaches. *Renew Energy* **1993**, *3* (4–5), 373–380. https://doi.org/10.1016/0960-1481(93)90104-O.
(42) Kambezidis, H. D.; Psiloglou, B. E.; Gueymard, C. Measurements and Models for Total Solar Irradiance on Inclined Surface in Athens, Greece. *Solar Energy* **1994**, *53* (2), 177–185. https://doi.org/10.1016/0038-092X(94)90479-0.
(43) Pandey, C. K.; Katiyar, A. K. Hourly Solar Radiation on Inclined Surfaces. *Sustainable Energy Technologies and Assessments* **2014**, *6*, 86–92. https://doi.org/10.1016/j.seta.2014.01.007.
(44) Iqbal, M. *An Introduction to Solar Radiation*; Academic Press, 1983.
(45) Kambezidis, H. D. The Solar Resource. In *Comprehensive Renewable Energy*; Letcher, T. M., Ed.; Elsevier: Oxford, 2022; Vol. 3, pp 26–117. https://doi.org/10.1016/B978-0-12-819727-1.00002-9.
(46) Gueymard, C. A. A Reevaluation of the Solar Constant Based on a 42-Year Total Solar Irradiance Time Series and a Reconciliation of Spaceborne Observations. *Solar Energy* **2018**, *168* (February), 2–9. https://doi.org/10.1016/j.solener.2018.04.001.
(47) Spencer, J. W. Fourier Series Representation of the Position of the Sun. *Search (Syd)* **1971**, *2* (5), 172.
(48) Acker, J. G.; Leptoukh, G. Online Analysis Enhances Use of NASA Earth Science Data. *Eos, Transactions American Geophysical Union* **2007**, *88* (2), 14. https://doi.org/10.1029/2007EO020003.
(49) Kambezidis, H. D.; Psiloglou, B. E. Climatology of the Linke and Unsworth-Monteith Turbidity Parameters for Greece: Introduction to the Notion of a Typical Atmospheric Turbidity Year. *Applied Sciences (Switzerland)* **2020**, *10* (11). https://doi.org/10.3390/app10114043.
(50) Perez, R.; Ineichen, P.; Seals, R.; Zelenka, A. Making Full Use of the Clearness Index for Parameterizing Hourly Insolation Conditions. *Solar Energy* **1990**, *45* (2), 111–114. https://doi.org/10.1016/0038-092X(90)90036-C.
(51) Kasten, F. A New Table and Approximation Formula for the Relative Optial Air Mass. *Archiv für Meteorologie, Geophysik und Bioklimatologie Serie B* **1965**, *14* (2), 206–223. https://doi.org/10.1007/BF02248840.
(52) Farahat, A.; Kambezidis, H. D.; Labban, A. The Solar Radiation Climate of Saudi Arabia. *Climate* **2023**, *11* (4), 75. https://doi.org/10.3390/cli11040075.
(53) Kafka, J. L.; Miller, M. A. A Climatology of Solar Irradiance and Its Controls across the United States: Implications for Solar Panel Orientation. *Renew Energy* **2019**, *135*, 897–907. https://doi.org/10.1016/j.renene.2018.12.057.
(54) Farahat, A.; Kambezidis, H. D.; Almazroui, M.; Ramadan, E. Solar Energy Potential on Surfaces with Various Inclination Modes in Saudi Arabia: Performance of an Isotropic and an Anisotropic Model. *Applied Sciences* **2022**, *12* (11), 5356. https://doi.org/10.3390/app12115356.
(55) Esbond, G. I.; Funmilayo, S. W. O. Solar Energy Potential in Yola, Adamawa State, Nigeria 2 The Problem 3 Literature Review. *International Journal of Renewable Energy Sources* **2019**, *4* (January), 48–55.

 doi:10.20944/preprints202305.0488.v1

(56) Raisz, E. The Analemma. *Journal of Geography* **1941**, *40* (3), 90–97. https://doi.org/10.1080/00221344108987724.
(57) Lynch, P. The Equation of Time and the Analemma. *Irish Mathematical Society Bulletin* **2021**, *0069* (69), 47–56. https://doi.org/10.33232/bims.0069.47.56.
(58) Kambezidis, H. D.; Larissi, I. K.; Nastos, P. T.; Paliatsos, A. G. Spatial Variability and Trends of the Rain Intensity over Greece. *Advances in Geosciences* **2010**, *26*, 65–69. https://doi.org/10.5194/adgeo-26-65-2010.
(59) Mueller, R.; Behrendt, T.; Hammer, A.; Kemper, A. A New Algorithm for the Satellite-Based Retrieval of Solar Surface Irradiance in Spectral Bands. *Remote Sens (Basel)* **2012**, *4* (3), 622–647. https://doi.org/10.3390/rs4030622.
(60) Farahat, A.; Kambezidis, H. D.; Almazroui, M.; Ramadan, E. Solar Potential in Saudi Arabia for Southward-Inclined Flat-Plate Surfaces. *Applied Sciences* **2021**, *11* (9), 4101. https://doi.org/10.3390/app11094101.
(61) Farahat, A.; Kambezidis, H. D.; Almazroui, M.; Al Otaibi, M. Al. Solar Potential in Saudi Arabia for Inclined Flat-Plate Surfaces of Constant Tilt Tracking the Sun. *Applied Sciences* **2021**, *11* (15), 7105. https://doi.org/10.3390/app11157105.
(62) Psiloglou, B. E.; Kambezidis, H. D. Estimation of the Ground Albedo for the Athens Area, Greece. *J Atmos Sol Terr Phys* **2009**, *71* (8–9), 943–954. https://doi.org/10.1016/j.jastp.2009.03.017.
(63) Hammad, B.; Al-Sardeah, A.; Al-Abed, M.; Nijmeh, S.; Al-Ghandoor, A. Performance and Economic Comparison of Fixed and Tracking Photovoltaic Systems in Jordan. *Renewable and Sustainable Energy Reviews*. December 2017, pp 827–839. https://doi.org/10.1016/j.rser.2017.05.241.
(64) Lazaroiu, G. C.; Longo, M.; Roscia, M.; Pagano, M. Comparative Analysis of Fixed and Sun Tracking Low Power PV Systems Considering Energy Consumption. *Energy Convers Manag* **2015**, *92*, 143–148. https://doi.org/10.1016/j.enconman.2014.12.046.
(65) Michaelides, I. M. M.; Kalogirou, S. A. A.; Chrysis, I.; Roditis, G.; Hadjiyianni, A.; Kambezidis, H. D. D.; Petrakis, M.; Lykoudis, S.; Adamopoulos, A. D. D. Comparison of Performance and Cost Effectiveness of Solar Water Heaters at Different Collector Tracking Modes in Cyprus and Greece. *Energy Convers Manag* **1999**, *40* (12), 1287–1303. https://doi.org/10.1016/S0196-8904(99)00020-5.
(66) Kambezidis, H. D.; Farahat, A.; Almazroui, M.; Ramadan, E. Solar Potential in Saudi Arabia for Flat-Plate Surfaces of Varying Tilt Tracking the Sun. *Applied Sciences* **2021**, *11* (23), 11564. https://doi.org/10.3390/app112311564.
(67) Drury, E.; Lopez, A.; Denholm, P.; Margolis, R. Relative Performance of Tracking versus Fixed Tilt Photovoltaic Systems in the USA. *Progress in Photovoltaics: Research and Applications* **2013**, *22*, n/a-n/a. https://doi.org/10.1002/pip.2373.
(68) Eke, R.; Senturk, A. Performance Comparison of a Double-Axis Sun Tracking versus Fixed PV System. *Solar Energy* **2012**, *86* (9), 2665–2672. https://doi.org/10.1016/j.solener.2012.06.006.
(69) Vaziri Rad, M. A.; Toopshekan, A.; Rahdan, P.; Kasaeian, A.; Mahian, O. A Comprehensive Study of Techno-Economic and Environmental Features of Different Solar Tracking Systems for Residential Photovoltaic Installations. *Renewable and Sustainable Energy Reviews* **2020**, *129*, 109923. https://doi.org/https://doi.org/10.1016/j.rser.2020.109923.